Design and fabrication of smart vaporizing liquid microthruster for Cubesat applications

by
Georgios Spernovasilis

July 2023

A thesis submitted to the Delft University of Technology in partial fulfillment of the requirements for the degree of

Master of Science in Electrical Engineering

Thesis committee: prof.dr. Lina Sarro
prof.dr. Angelo Cervone
Dr. Henk W. van Zeijl

The work in this thesis was made in:

ECTM
Faculty of Microelectronics
Delft University of Technology

Abstract

Propulsion systems capable of providing attitude and orbit control are an essential part of small satellites. In particular, Micro-Electro-Mechanical Systems (MEMS) Vaporizing Liquid Microthrusters (VLM), using water as a propellant, meets the requirements for launch-safety, simplicity and cost. Moreover, MEMS technology also enables the integration of sensors to fabricate smart thrusters. This thesis reports the design and fabrications of a smart vaporizing liquid microthruster for the applications in small satellites. The thruster is fabricated with a conventional anodic bonded silicon-glass wafer stack with a glass capped microfluidic channel but the novelty here is that in-channel heaters and sensors on the glass wafer are combined with on-channel heater and sensors on the silicon wafer. For example, an on-silicon piezo resistive pressure sensor is combined with an in-channel temperature sensor. To enable close proximity and stacking of heaters and sensors, a combined front-side/back-side silicon wafer processing is applied. Furthermore, the on-silicon heater is built in a recess on the silicon wafer to minimize thermal resistance between heater and channel. The modular designed layout allows the integration of different sensor / heater combinations in the wafer stack to meet an application specific thruster performance, which enables cost effective flexible manufacturing. A preliminary characterization was performed which showed that integration of all designed modules was successful. The proposed fabrication process could therefore be a fabrication platform for VLMs.

Contents

1 Introduction **1**
1.1 Project background . . . 1
1.2 VLM overview . . . 2
1.3 Literature review . . . 4
1.4 Boiling instabilities . . . 5
1.5 Active control of flow instability . . . 6
1.6 Scope of thesis . . . 7

2 Heater **8**
2.1 Resistive micro-heater . . . 8
2.1.1 Material choice . . . 9
2.1.2 Resistor shapes . . . 10
2.1.3 Heat transfer modes . . . 10
2.1.4 Transient heat flow . . . 12
2.2 Design overview . . . 13
2.3 FEM simulations . . . 14
2.3.1 Heat transfer simulations . . . 14
2.3.2 Mechanical simulations . . . 17
2.4 Conclusion . . . 19

3 Vapor fraction sensor **20**
3.1 Theory and design . . . 20
3.1.1 Capacitance . . . 20
3.1.2 Dielectric permitivity of water . . . 21
3.1.3 Inter-digital capacitor design . . . 22
3.1.4 FEM simulations . . . 22
3.2 Conclusion . . . 27

4 Pressure sensor design **29**
4.1 Pressure sensors . . . 29
4.2 Membrane design . . . 29
4.3 Piezoresistor design . . . 30
4.4 Temperature compensation . . . 31
4.5 Design overview . . . 32
4.6 FEM simulations . . . 33
4.6.1 Conclusion . . . 37

5 Processing **39**
5.1 Modular fabrication . . . 40
5.2 Frontside processing . . . 41
5.3 Backside processing . . . 42
5.4 Glass processing . . . 43
5.5 Anodic bonding . . . 43
5.6 Critical steps and problems . . . 44
5.6.1 wafer bonding . . . 44
5.6.2 Delamination of photo-resist layer . . . 44
5.6.3 Broken oxide membranes on inlet holes and bonding cavities . . . 45
5.6.4 Mask undercut . . . 45
5.6.5 DRIE . . . 45
5.7 Assembly . . . 46
5.7.1 PCB attachment . . . 46
5.7.2 Connection to microfluidic interface . . . 46
5.8 Summary . . . 47

6 Characterization **48**
6.1 Sensor calibration 48
6.1.1 RTD/heater characterization 48
6.1.2 Vapor fraction section calibration 49
6.1.3 Pressure sensor Calibration 50
6.2 Heater performance 51
6.3 Flow observations 54
6.4 Conclusion 55

7 Summary **57**
7.1 Future work 57

A Appendix **62**

B Appendix **65**

1 Introduction

1.1 Project background

Over the past twenty years, there has been a shift from a select group of countries, space agencies, and large industries building, launching, and operating satellites and other spacecraft to a scenario where many universities and research institutes are able to do so. Advancements in microelectronics have reached a level in which satellites with significant functionality could be fitted in a very small volume. In addition the availability of micro-controllers, which are system-on-chips requiring less than a Watt to operate, have been a key enabler to this development. The "Cube-sat" standard ,introduced in 1999 defined a class of miniaturized satellites with standard dimensions of $10cmx10cmx10cm$ that typically weigh less than 1.33 kg. Due to their small size cubesats can be launched as part of a larger mission without additional costs and could therefore offer a cost effective solution to replace conventional bulky commercial satellites .In 2013 interest in the commercial sector started rising rapidly with two companies [1] running 100+ cube-sat constellations for optical imaging and weather prediction .More recently a similar rise was observed in the telecommunication and astronomical scientific sectors.

To enhance the capabilities of Cubesats micro-propulsion systems are currently being developed. With the integration of propulsion systems Cubesats can achieve active attitude control, reaction wheel desaturation, drag recovery, orbit changes and proximity operations [2]. With the aid of an effective propulsion system the orbital decay of a CubeSat can be slowed down and its lifetime increased. Furthermore, Cubesats can work cooperatively in swarms to form virtual antenna arrays to realize a larger aperture area with higher reliability.

The following propulsion technologies have been applied on current CubeSat missions: solar sail, cold gas, electric propulsion systems, and chemical propulsion systems [3]. Advancements in mems technologies create great opportunities for further development of these systems. The reduction in power consumption that comes from the miniaturization function of micro-fabricated structures can help comply with the power limitations of small sattelites. Further miniaturization is possible with mems and microfluidics devices because they interface so well with each other and with microelectronics. Integration of sensors becomes possible which is crucial to make them more efficient and applicable to a wider range of missions. Monolithic integration of sensors directly coupled to thruster performance along with power electronics and microfluidics leads to significant improvements in robustness. An overview of mems propulsion systems developed for nanosattelites is shown in table 1.

One of the more promising options is the VLM, which not only has good performance but also can operate on safe, cheap and environmentally friendly propellants. This is often a requirement for propulsion systems in nanosatellites as they are often launched through "ride-sharing" as part of a larger mission and are required to not add any additional safety hazards. Additional advantages of the VLM are its relatively simple fabrication which could be done using conventional MEMS techniques, small volume, low mass, fast response, high thrust to mass ratio, high reliability, and easy integrability in a thruster array. In addition, they can easily achieve a thrust level in the range of 1–10 mN with a specific impulse in the range of 50–200 s, and a reasonably low power consumption.

Types of microthrusters	Performance	Advantages	Disadvantages
Solid propellant microthrusters	Thrust:>100mN Specific Impulse:<100s	Easy propellant loading, no leakage of propellant, low cost and power consumption	One-shot use, lack of restart ability, and combustion instability
Liquid monopropellant microthruster	Thrust:0.3-200mN Specific Impulse:5-180s	Small demand for electricity, simplified fabrication and low cost, non-toxic combustion products.	Propellants are easily to decompose, heat preservation, and ventilation of storage tanks.
Vaporizing liquid microthruster (VLM)	Thrust:0.03-10mN Specific Impulse:3.42-105s	Simple structure, low voltage, low cost and easy to fabricate, no pollution of propellants	Too difficult to reach more than 1mN of thrust, relatively small level of specific impulse
Cold gas microthruster	Thrust:0.8-2.24mN Specific Impulse:<50s	Simple structure, reliable, low energy consumption, and easy to be miniaturized	Needs high pressure gas storage tank, large volume and weight, difficult to prevent leakage

Table 1: MEMs microthrusters

1.2 VLM overview

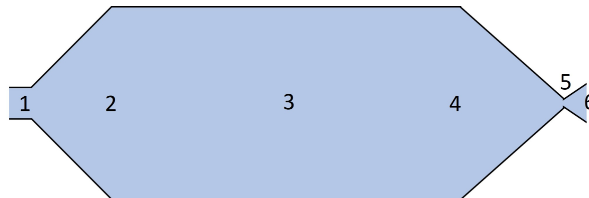

Figure 1: Schematic of VLM thruster with numerated modules

1. Propelant inlet
2. Divergent inlet section
3. Heating chamber
4. Nozzle convergent area
5. Nozzle throat
6. Nozzle diverging area

The VLM consists of a pressurized tank, a valve for flow control, a vaporization chamber and a nozzle. Liquid flow created by the pressurized tank and the valve is forced through the vaporization chamber where it vaporized and the super-heated vapor is accelerated to supersonic speeds as it flows through the converging nozzle producing thrust. An overview of the VLM modules is shown below:

Inlet

The inlet section includes the micro-fluidic interface between the propellant tank the VLM and the inlet chamber. The main design considerations for the inlet are: fully developed flow at the entrance of the vaporization chamber, reduced back-flow, mechanically robust fluidic interface that can withstand high temperatures, temperature cycling and the g-forces at launch.

Vaporization chamber

In the vaporization chamber heat is delivered from an external or internal micro-heater to the fluid . Heat must be transferred efficiently and uniformly while minimizing pressure losses. In

literature two types of types of heating chambers can be distinguished, those with planar heaters and those than include an internal channel structure. Internal channel geometries have been investigated as a method to increase heat transfer in microfluidic heat-sinks by improving the thermal contact to the fluid.

Nozzle

Thrust is created as vaporized propellant is propelled towards the throat and pushed out of the VLM. The geometry of the nozzle typically consists of a converging and a diverging section and is critical in determining how propellant exits the chamber. The nozzle should be designed in such a way that liquid exiting the throat of the nozzle achieves the highest allowable speed to generate high thrust. Depending on the propellant and thrust requirements, the VLM could incorporate linear or aerospike nozzles. In this project the design of the nozzle is not considered. A linear converging diverging nozzle is instead integrated in the design in order to test the concepts of the heating chamber and inlet but nozzle parameters affecting thrust are not investigated.

VLM Performance

Thrust produced by the VLM is described by:

$$F = \dot{m}v_e + (p_e - p_a)A_e \tag{1}$$

where $\dot{m}$ is the mass flow rate, p_e is the pressure at the nozzle exit ,p_a is the ambient pressure and u_e the exit velocity. Two components can be distinguished in the thrust equation, a velocity term and a pressure term. Equation 1 can be rewritten to express the produced thrust as a function of the pressure in the vaporization chamber P_c:

$$F = C_f P_c A_t \tag{2}$$

where the C_f is the thrust coefficient given by:

$$C_f = \Gamma \sqrt{\frac{2\gamma}{(\gamma+1)}[1 - \frac{p_e}{p_c}^{\frac{\gamma-1}{\gamma}}]} + \frac{A_e}{A_t}(\frac{p_e - p_a}{p_c}) \tag{3}$$

$$\Gamma = \sqrt{\gamma(\frac{2}{\gamma+1}^{(\gamma+1)(\gamma-1)})} \tag{4}$$

Where γ is the ratio of specific heat between gas and liquid phase, A_e is the area of the nozzle exit and A_t the area at the nozzle throat. From equation 2 the produced thrust of the vlm is proportional to the throat expansion ratio. However increasing the expansion rate of the produced vapor above a certain value leads to the occurrence of supercooling causing the vapor to condense and produce ice which deteriorates the performance and could block the nozzle exit. The issue of supercooling can be prevented by ensuring that the vapor is sufficiently super-heated in the vaporization chamber since higher temperature steam condenses less rapidly. The nozzle must therefore be designed taking the vaporization chamber performance and available power into consideration in order to achieve the maximum attainable thrust.

Another important performance characteristic of the VLM is its propellant efficiency or specific impulse defined as:

$$I_{sp} = \frac{F}{\dot{m}} \tag{5}$$

Minimizing the pressure drop inside the vaporization chamber is crucial for achieving High I_{sp} since the second term in the thrust equation is proportional to the pressure at the nozzle throat. The maximization of the thrust force F, the maximization of the specific impulse I_{sp}, and the minimization of the power consumption P_d for propellant vaporization and overheating are the three key steps that drive the performance optimization of a VLM. These can all be combined into overall efficiency parameter

$$h_o = g_0 I_{sp} \frac{F}{P_d} \tag{6}$$

The choice of propellant is also vital for the overall performance of the vlm. The amount pressure drop caused by viscous losses is described by the Reyhnolds number which is given by:

$$Re = vD\frac{p}{\mu} \tag{7}$$

Propellant	Formula	Molecular Weight (kg/Kmol)	Liquid Density (g/cm^3)	Latent heat of Vaporization (kj/kg)	Prandtl number (liquid phase)
Ammonia	NH_3	17	0.6	1159.7	1.38
Propane	C_3H_8	44.1	0.49	339.3	3.48
Acetone	C_3H_6O	58.08	0.784	518	4.5
Butane	C_4H_10	58.1	0.57	360.2	3
Freon 12	CCl_2F_2	120.9	0.98	141.8	3.5
Water	H_2O	18	1	2442.5	6.9
Hydrogen Fluoride	HF	20.1	0.99	1505.9	4.41
Methanol	C_2H_3OH	44	0.79	1099.3	6.83

Table 2: Properties of different propellant options for resistojets

Where μ is the fluid dynamic viscosity p is the fluid density, v is the velocity and D the hydraulic diameter of the channel. Furthermore material properties of the propellant are present in the Nusselt and Prandtl number equations which are crucial quantities for the evaluation of heat transfer performance. The Prandtl number is a dimensionless number given by:

$$P_r = \mu \frac{C_p}{k_f} \tag{8}$$

where k_f is the heat conductivity and C_p the specific heat that is an intrinsic property of a fluid. Fluids with small Prandtl numbers are free-flowing liquids with high thermal conductivity and are therefore a good choice for heat conducting liquids. The Nusselt number is an important parameter that contributes to a better rate of heat exchange. It is basically a function of Reynolds and Prandtl number. The correlation is provided in 9.

$$N_u = h\frac{D}{k_f} = 0.666 Re^{0.5} Pr^{1.3} \tag{9}$$

Where h is the convective heat transfer coefficient. k_f is the thermal conductivity of the fluid and C_p is the specific heat. The nusselt number is the ratio between conductive and convective heat transfer coefficients and can be used to quantify the thermal contact to the fluid. When a fluid that is less viscous and less conductive the vaporization chamber must be designed with a higher heating area to volume ratio in order to achieve the same amount of heat transfer. In addition to the heat transfer efficiency another parameter that contributes to the overall power efficiency and I_{sp} of the VLM is the total power needed to reach vaporization which is dependent on the boiling incipience temperature and latent heat of vaporization. An overview of the promising propellant options is shown in table 2.

. Given its comparatively low molecular mass, inherent safety, non-toxicity, and cheapness, water has the potential to be a excellent proppelant, especially for small spacecraft like Cubesats. It is easily storable and its relatively high density allows for smaller tank volume when compared to other propellants. However, the high specific heat and high latent heat of vaporization of water are two important limiting factors for the efficiency of the system.

1.3 Literature review

Several VLM demonstrators have been reported in literature with thrust outputs ranging from 5 μN to 4 mN. Vaporizing chamber designs found in literature can be grouped into different categories based on the type of heater (internal or external) and the microfluidic channel configuration (single channel , parallel channels, internal fin structures). Internal heaters , fabricated inside the microfluidic channel are more efficient compared to external ones. However they are more challenging to manufacture since connection of the external wires and ensuring fluidic tightness of the device becomes more complicated. The first VLM was developed by Muller et al. [4] who manufactured a vlm with an internal diffused silicon heater, the vaporization chamber was micro-machined in glass and capped on both sides with silicon through anodic bonding. Maurya et al. [5] developed a silicon-based VLM with an integrated p-diffused microheater and

two bonded micro-machined silicon chips. The internal heater was fabricated on the bottom silicon substrate by diffusing boron, and the p-diffused resistive heater was passivated by thermally grown silicon dioxide. Ye et al. [6] proposed a VLM concept which explosively vaporized water by applying high power electric pulses. The microthruster fabricated on two silicon wafers and includes a internal titanium resistor passivated with silicon oxide, electrical connections to the Ti resistor was made through a hole in the silicon wafer which was sealed with glue. In addition silicon was removed from the backside of the heater to reduce its thermal mass and allow a faster response. More recently kwan et al [7]. fabricated a VLM with an internal molybdenum microheater that operates in the film boiling regime. By applying power that exceeds the critical heat flux condition the liquid propellant does not come into contact with the channel walls minimizing friction losses and achieving very high I_{sp}. The main challenge in the fabrication of internal structures is that the electrical connections can compromise the fluidic tightness of the device. Liu et al. [8] solved this problem with the implementation of inductive heating, eliminating the need for connection of external wires and ensuring channel sealing. Another promising solution to ensure sufficient fluidic tightness was demonstrated by [9] who used thermo-compressive bonding with an aluminum adhesion layer which was patterned around the internal structures to create a more flat topography.

Compared to internal heaters, external heaters lose more heat to the surrounding substrate because the paths of thermal transfer from the heater elements to the propellant become more indirect and thus limiting the thermal efficiency, but significantly simplify the fabrication process of the VLM. VLMs with external heaters were reported in [9]-[13]. Kundu et al [10], fabricated a single channel vaporization chamber using silicon to silicon adhesive bonding and included two external heaters for more uniform heating. Cen and Xu [11] first fabricated a VLM with parallel microchannels for improved contact to the propellant and described the occurrence of boiling instabilities. The channels were capped with anodically bonded glass. Glass compared to silicon is a very poor heat conductor and therefore results in lower heating contact area, however it provides optical access into the microfluidic channel and observation of the boiling instabilities which is a very crucial aspect of VLMs. In recent design studies on vaporizing liquid microthruster ([12], [13], [14]), various heat transfer enhancement features such as circular and diamond-shaped pedestal arrays and serpentine channels, mainly to maximize the thermal contact area of the vaporization chamber for more efficient heat addition, have been examined.

1.4 Boiling instabilities

One of the most crucial aspects of the VLM is the presence of boiling instabilities which severely deteriorates their performance and limits their applicability. Boiling instabilities can be characterized by uneven distribution of propellant between channels, pressure and temperature fluctuations, and intermittent flow reversal. In VLMs boiling instabilities manifest as fluctuations in thrust output. As can be observed in figure 2 the pressure signal strongly couples with the thrust output signal which oscillates at a similar frequency and phase. Two types of boiling instabilities can be distinguished in two phase microfluidics, those related to pressure instability and those related to explosive boiling. The pressure drop instability that transpires during boiling is a result of the interaction between the vapor within the channel and the compressible volume upstream. Under constant heating the amount of vapor in the microfluidic channel will vary. Increased vapor generation in the microfluidic channel increases flow resistance and increased flow resistance reduces flow rate. And because of the lower flow rate the upstream pressure increases and a periodic condition can be established. Another type of instability stems from the rapid bubble growth and channel clogging. The rapid-bubble-growth instability is observed in microscale flow boiling systems because the small characteristic channel sizes confine vapor bubbles formed during boiling. This confinement causes the bubbles to significantly influence the operating characteristics of the system, and can cause pressure fluctuations and reverse flow. Explosive boiling is often observed on the edges of internal fin structures where the nucleation temperature is lower. The inertial forces caused by the rapid expansion of vapor pushes the liquid in both directions and causes flow fluctuations. When explosive boiling takes place in the inlet chamber, flow reversal instability occurs in microchannels. In a VLM composed of parallel microchannels, more complex two-phase flow dynamics are observed. Parallel channel instabilities are established due to the presence of the inlet chamber. Explosive boiling at the entrance of the parallel channels where the edges are sharp causes backflow. Furthermore, uneven distribution

of propellant between channels caused by channel clogging leads to additional flow and pressure instabilities.

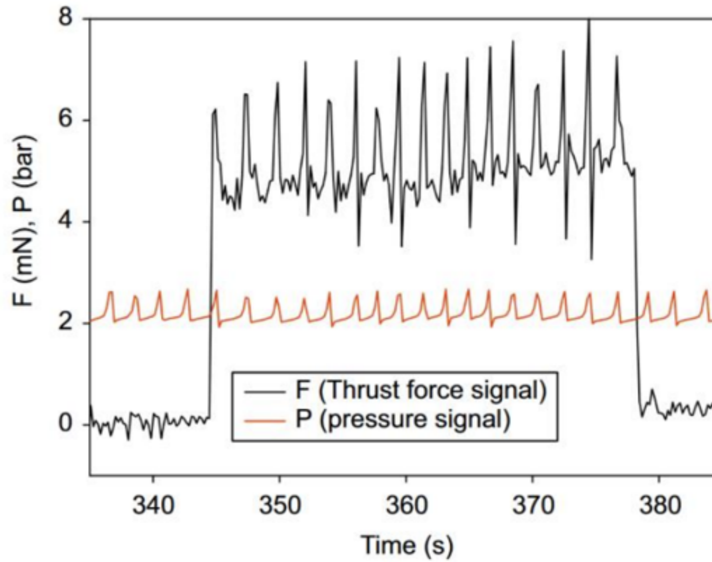

Figure 2: Thrust and pressure fluctions in single channel VLM [11]

1.5 Active control of flow instability

The effect of the heat flux and flow rate on boiling instabilities has been extensively studied in literature. Wang et al. [14] studied the stable and unstable flow characteristics in single as well as parallel micro-channels of trapezoidal section having equal hydraulic diameters and characterized the stability of the flow with respect to applied heat flux and mass flow rate. Operation in a certain range of heat and mass flux conditions was shown to result in stable flow meaning, negligible temperature and pressure oscillations. [16] investigated the effect of flow oscillations on the temperature and flow distribution in an evaporator with two parallel micro-channels. Results showed that in the presence of flow oscillations caused by pressure drop instability during flow boiling, flow redistribution occurs between the two channels resulting in more uniform flow and temperature distribution. Although flow oscillations are generally undesirable, artificially induced oscillations(not relying on pressure drop instability) could be a viable method of enhancing the heat transfer in microfluidic channels. The effect of pulsed heating on flow oscillations was investigated by [18] who experimented with application of flux pulses and demonstrated that at heating frequencies between a certain range, the flow boiling instabilities and performance heavily couple to the temporal profile of the heat flux, causing the pressure drop oscillation frequency to match the heating pulse frequency. Furthermore application of pulsed heating has shown promising results with respect to heating efficiency enhancement. At the onset of boiling, the dynamic response resembles that of an under-damped mass-spring-damper system subjected to a unit step input. During transitions between single-phase flow and time-periodic flow boiling, the wall temperature temporarily over/under-shoots the eventual steady operating temperature thus demonstrating that transient performance can extend beyond the bounds of steady performance. An example of the temperature response to a step input is shown in figure 3. Consequently, thermal performance could be potentially dramatically increased by applying the heat flux in a periodic manner at a frequency which matches with the resonance frequency of the second order thermal system. Furthermore, compared to the one with single-phase flow, the micro-channel experiencing time-periodic boiling can withstand a longer high-heat flux pulse, even with the higher temperature at walls prior to the pulse [19]. Attempts to eliminate the stochastic nature of boiling have been made by employing artificial nucleation sites and bubble seeding [21]. A thermally isolated heater generates bubbles of small dimensions which are then fed into the vaporization chamber and begin to grow. This method of separating bubble nucleation and bubble growth simplifies the heat transfer system and allows precise control of the flow patterns and heat transfer.

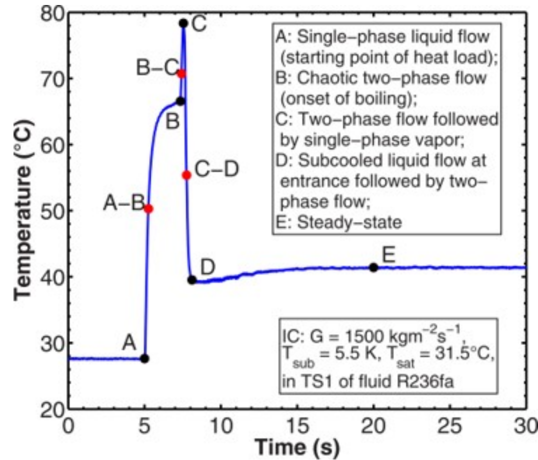

Figure 3: Wall temperature variation versus time from a step input [17]

Active control of the heat flux has shown promising results with respect to heating efficiency and oscillation control. To optimize the application of heat flux the use of feedback from integrated sensors can be very beneficial. Fontanarosa et al. [20] designed and fabricated a VLM equipped with embedded micro-sensors for real-time monitoring of the in-channel vapor/liquid fraction and fluid temperature during its operation. Further, a secondary resistive heater was placed inside each of the eight channels, allowing for localized fluid heating. Integration of thermally isolated internal temperature sensors allows direct measurement of the fluid temperature and a direct way of evaluating thermal efficiency. The percentage of vapor at various points along the channel is correlated to the local heat transfer. Feedback from vapor sensors in combination with localized heating can be used to tune the heat flux distribution along the channel to enhance the overall heat transfer and control the stream. Finally, information about the pressure gradient across the vaporization chamber is the primary indication of the design quality of the microfluidic channel since large pressure drops can result in huge loss of thrust. Furthermore, the transient pressure signal is extremely usefull for control of the input power and flow rate in the VLM since it is closely correlated to the thrust output.

1.6 Scope of thesis

In this work a MEMS micro thruster design and fabrication process is proposed that facilitates the implementation of active control of the heat flux by providing fast temperature response and localized heating. Microfluidic channels are etched in silicon and capped with glass .Pressure, temperature and vapor fraction sensing in the microfluidic channel is monolithically integrated on both sides of the channel to accurately characterize the vaporization behavior and to allow the development of an effective heating strategy. To accommodate the combined integration of different types of sensors on one device it is desirable that the sensors are designed as planar structures that can be placed on either side of the channel allowing their parallel integration and thereby reducing the channel length and corresponding fluidic resistance. Heaters and sensors are designed as separate modules of equal dimensions ($1mmX6.2mm$). Using waferstepper lithography and multi-image photomasks, different configurations can be placed on the wafer using one photomask. The modular designed layout allows the integration of different sensor / heater combinations in the wafer stack to meet an application specific thruster performance, which enables not only rapid prototyping but also cost effective flexible manufacturing.

2 Heater

Typical designs of integrated heaters in MEMS devices make use of electrically conductive thin films. These can be deposited polycrystaline semiconductor layers, thin metal films or diffused layers in silicon. Power can be generated either Ohmicly or inductively . Inductive heating has been was demonstrated in VLM applications in [8] and is a promising option for internal heating in a microchamber because it doesn't require connection of external wires that could compromise the channel sealing. Ohmic heating however is a more more direct way of power delivery in which 100% of the electrical energy is converted into heat. Furthermore, resistive heating allows temperature measurements by monitoring variations in resistance and has a faster response time. Resistive heaters integrated into single crystalline silicon by diffusion or ion implantation have a limited operating range because of the low bandgap energy of silicon. Metals heaters offer good mechanical properties high thermal conductivity and high liniarity with respect to temperature. In the following subsections the theory and design of a vaporization chamber that draws power from metalic resistive microheaters will be discussed.

2.1 Resistive micro-heater

Heat is supplied to the propellant through electric power dissipation in a resistive heater. The amount of heat dissipated is given by:

$$P = \frac{V^2}{R} \tag{10}$$

The resistance of a resistor with a rectangular shape shape can be expressed by:

$$R = \rho \frac{L}{tA} \tag{11}$$

Where L is the total length ,A the cross sectional area, t is the layer thickness and ρ the resistivity of the heater material. The resistive micro-heater can also be used as a temperature sensor by exploiting its temperature coefficient of resistivity (TCR). The dependence of the resistance with temperature is expressed by:

$$R_t = R_0(1 + a(T - T_0)) \tag{12}$$

For larger temperature ranges this first order approximation might not be valid and a more accurate characterization of the resistance is needed as described by the Callendar van Dusen equation.

$$R_t = \begin{cases} R_0[1 + AT + BT^2 + C(T-100)T^3], & T < 0^oC \\ R_0[1 + AT + BT^2], & T > 0^oC \end{cases} \tag{13}$$

which also includes second and third order terms, R_0 is the temperature at 0^oC. This method of resistive temperature measurement is chosen because of its high linearity and fast response time it also enables heater and temperature sensor integration on one device. A comparison of different temperature methods is shown in table 3. By applying constant current and measuring the voltage drop through a four point measurement the resistance of the connecting wires can be canceled out.

Attribute	RTD	Thermocouple	Thermistor	Silicon IC
Temperature Range	-200 to 850°C	-184 to 1260°C	-55 to +150°C	-55 to +125°C
Linearity	Excellent	Fair	Poor	Good
Thermal Response Time	Fast	Fast	Moderate	Slow
Precision	Excellent	Fair	Poor	Fair

Table 3: Temperature measurement methods

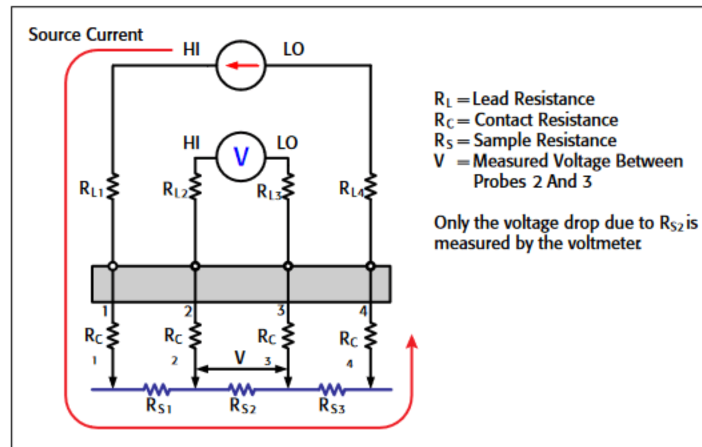

Figure 4: 4 probe resistance measurement setup

Performance criteria that can be divided into two groups are generally used to characterize micro-heaters. Parameters concerning the mechanical robustness and stability which include mechanical stress, thermal stress, stress distribution. And the second category which is related to heat generation and includes: uniformity, accuracy, stability, power consumption, and response time. These performance parameters depend on the micro-heater geometry, the materials chosen for the heater, substrate and process conditions.

2.1.1 Material choice

Metals typically used for high temperature applications are Titanium, Molybdenum, Platinum and Tungsten. Table 4 the maximum operating temperatures reported in literature for heaters of different heater materials. The maximum operating temperature of a micro-heater depends on the linearity of the material properties and on weather the heater comes in direct contact with oxygen, as metals become increasingly prone to oxidation as the temperature increases. Although contact with oxygen typically isn't relevant for application in space it will be part of the experimental conditions in this project. Furthermore, similar devices are commonly packaged through air gap packaging in which atmospheric air is used as a heat insulator.

Microheater material	Molybdenum	Titanium	Platinum	Tungsten
Maximum operating Temperature	320 ^oC	700 ^oC[29]	550 ^oC[27]	600^oC[28]

Table 4: Maximum operating temperature of micro-heaters of different materials as reported in literature

Regarding the mechanical stability of micro-heaters placed on flexible membranes low Young's modulus and high maximum tensile strain are desired. Thermal stress can be minimized by choosing a material with low temperature expansion coefficient (TEC), close matching between the TEC of the heater material and the insulating layer which can be either SiN or SiO_2 and high thermal conductivity.

Regarding the heat generation parameters the electrical resistivity of the resistive layer should be high in comparison to the contact pads so that efficient Joule heating occurs at the resistor, and the unwanted heat in the contact pads is minimized. Accuracy and stability largely depend on the linearity and sensitivity of the material properties with regards to temperature. Fast response time requires low resistivity and low thermal mass.

Platinum is often chosen as a heater material for internal channel heating because of its inert nature however because of its poor adhesion with glass it requires a titanium or chromium adhesion layer. Molybdenum's high melting point and TCR also make it a good candidate. However as its not a cmos compatible material processing is more complicated in a standard cleanroom. Furthermore it becomes prone to oxidation above 320^oC and requires a protective layer. Titanium has been reported to operate at temperatures up to 700 ^oC has high accuracy and simple

processing and is the chosen material for this work. Unlike, platinum titanium can react with liquids hence for in-channel applications a protective layer such as SiO_2 is required.

2.1.2 Resistor shapes

The most common resistor layout is serpentine, which consists of straight long tracks alternatively connected in series by short connecting segments with sharp 180 turns. This configuration possesses a constant heating power per active area which inevitably induces a hot spot in the heater center. Unlike serpentine layout, a spiral configuration involves straight long tracks with many 90 turns. It has been demonstrated that the heating power within the active area can be adjusted either by varying line-width [23] or varying spacing [24] or varying line-width and spacing simultaneously [25]. In [25] a two dimensional approach was used to optimize the temperature uniformity in both the transverse(across the tracks) and longitudinal(along the tracks).

Since the heater is placed on a flexible membrane the maximum stress and stress distribution on the resistive layer is a point of concern. In order to minimize stress concentrations sharp corners should avoided and a structure should be employed that enables the release of stress. Also the sensitivity of the resistance with respect to stress is dependent on the geometry and can be controlled by employing serpentine designs as was demonstrated in [26]. A comparison of the relative change in resistance due to strain in straight line and serpentine resistor structures is shown in figure 5. Increasing the angle of the turn in serpentine structure results in lower sensitivity to strain. The heater metal should be sufficiently thick as layers become stiffer with increasing thickness. Both the line-width in the serpentine structure and the layer thickness must be optimized to achieve the required mechanical robustness while also meeting the resistance and temperature distribution requirements.

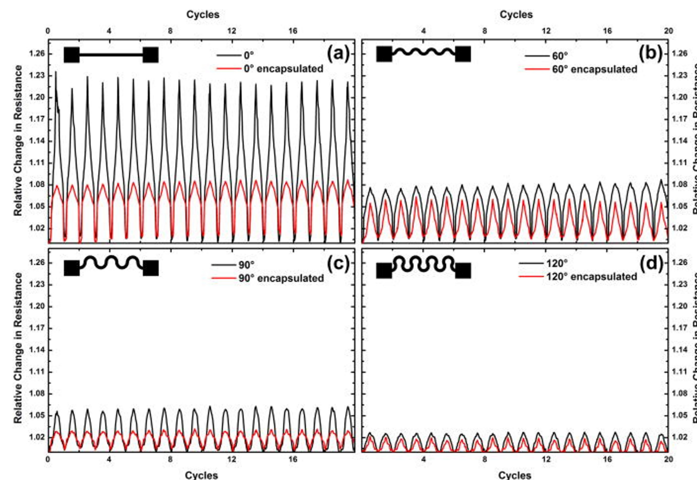

Figure 5: Sensitivity of resistance with respect to stress for straight line and serpentine resistors. [26]

2.1.3 Heat transfer modes

Heat is transferred away from the heater through

- Forced convection to propellant

$$Q = h_{fluid}(T_{wall} - T_{fluid}) \tag{14}$$

- lateral conduction, conduction to substrate

$$Q = k\Delta T \tag{15}$$

- natural convection to air

$$Q = h_{air}(T_{surface} - T_{air}) \tag{16}$$

- radiation to ambient

$$Q = \sigma\epsilon(T^4 - T_{amb}^4) \tag{17}$$

Where k is the thermal conductivity, h_{air},h_{water} are the heat transfer coefficients to air and water respectively, T_{wall} is the temperature of the internal channel walls, T_{fluid} is the temperature of the fluid and $T_{ambient}$ the ambient temperature. For each of the above heat transfer modes the resistance offered to the heat rate and is defined by:

$$R = \frac{\Delta T}{Q} \tag{18}$$

For heat conduction through a solid the rate of flow of heat is proportional to the cross-sectional area A and the temperature gradient. Thus, for two points at temperatures T1 and T2 and a distance L apart,

$$R = \frac{L}{kA} \tag{19}$$

The thermal resistance for convection is

$$R = \frac{1}{Ah} \tag{20}$$

Where A is the contact are of the heated area with the fluid.

Equations 16,17 describe the heat losses to surrounding environment. Convection to air is not relevant for a microthruster operating in space as convection to air doesn't exist in vacuum however it will be present in the experimental conditions of this project. Radiation losses only need to be considered at high temperatures since the temperature dependency only includes a fourth order term. Furthermore the radiation loss can be greatly mitigated with appropriate packaging. Package of the VLM has to be constructed from a material with low surface emissivity at the outside and from the side looking at the heater it needs to be reflective. The heat resistance between the heater and the ambient environment is proportional to the total chip area. Regarding the heat removed by the propellant, the heat transfer coefficient h is inversely proportional to the characteristic length of the channel, which for a rectangular micro-channel with a width much larger than its height can be defined as the channel depth. However reducing channel height does not necessarily improve heat transfer because of the viscous dissipation at the channel walls. Viscous dissipation causes the temperature of the fluid to increase near the channel wall decreasing the temperature difference between wall and propellant and leading to a decrease in heat transfer. A numerical study presented in [30] showed that for rectangular water filled micro-channels reducing the hydraulic diameters below $50\mu m$ does not offer an improvement in heat transfer due the the frictional heating of the channel walls. The friction factor ($f = 64/R_h$) as a function of the channel hydraulic diameter is shown in figure 6. The corresponding pressure drop as a function of the channel length is given by:

$$p = \lambda(\frac{L}{D_h})(\frac{\rho\mu^2}{2}) \tag{21}$$

For the design of a microthruster a large pressure drop inside the channel is not desired as it directly affects the produced thrust. According to the Gouy-Stodola theorem the lost power can be calculated by

$$W_{lost} = T_{amb}S_{gen} \tag{22}$$

Where S_{gen} is the entropy generation rate. When the heat flux applied at the channel walls exceeds the critical heat flux only vapor is in contact with the wall causing a reduction in pressure loss due to the lower kinematic viscosity of water vapor. The energy loss becomes more severe at higher temperature since as can be seen from the Temperature-entropy diagram for water vapor the isobaric lines diverge as the temperature increases meaning that at higher temperatures a drop in pressure causes a larger change in entropy. Equation 22 shows the relation between loss in output power of the thruster and pressure drop in the vaporization chamber. For a mass flow rate of 1 mg/s the pressure drop corresponding to a hydraulic diameter of 194 μm and a channel length of 1mm is .002 Bar for vapor at a temperature of 420 K and 0.015 $bar$for saturated liquid water .The corresponding change in entropy is 0.002 kJ/Kg and 0.003 kJ/Kg. Assuming an ambient temperature of 293 K in experimental conditions the lost power is 7 mW for liquid water and 50 mW for water vapor at 420 K.

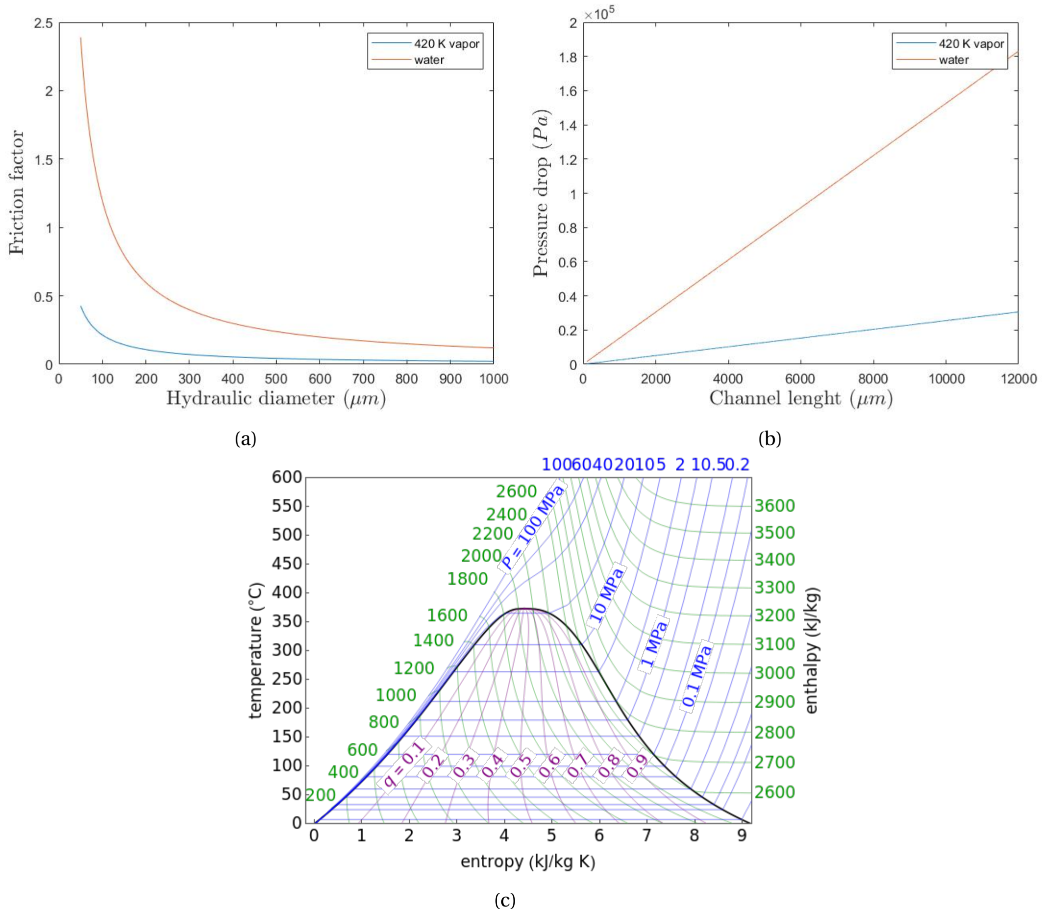

Figure 6: a)Darcy-weisbach friction factor as a function of the channel hydraulic diameter b) Pressure drop for a microchannel with a hydraulic diameter of 200 μm c) Entropy temperature diagram

For a given flow rate minimum power required to reach a point of vaporization and further increase the liquid temperature is determined by the following equations:

$$Q_1 = \dot{m}c_p(100^oC - T_i) \tag{23}$$

$$Q_2 = \dot{m}L_u \tag{24}$$

$$Q_3 = \dot{m}c_p(T_v - 100^oC) \tag{25}$$

Where T_i is the subcooled temperature, c_p the specific heat of the water, $\dot{m}$ the mass flow rate and T_v the vapor temperature. The overall power efficiency of the vaporization chamber is expressed as:

$$\eta = \frac{P_{Liquid,\Delta T} + P_{vapor,\Delta T} + P_{latent}}{P_{input}} \tag{26}$$

2.1.4 Transient heat flow

In steady state conditions heat transfer can be modeled as a resitive network. However when transient heating is considered another important parameter that needs to be included is heat capacitance. When the heat rate supplied to mass volume changes from Q_1 to Q_2 the transient temperature response is described by:

$$Q_1 - Q_2 = C\frac{dT}{dt} = c_p m\frac{dT}{dt} \tag{27}$$

.An accurate lumped electrical model can be created by splitting the volume in to parts that can be considered to be at uniform temperature. Pieces that can be represented by a single heat

capacity can be identified by a low BIOT number defined as the ratio between the body volume and the heated (or cooled) surface of the body:

$$Bi = \frac{h}{k}L \tag{28}$$

Where L is the characteristic length typically defined as:

$$L = \frac{V}{A_Q}. \tag{29}$$

Where A_Q is the area through which heat flows. Parts which have high Biot numbers may be split into smaller pieces, connected to each other by a thermal coupling, such that the Biot number of individual pieces is sufficiently low (Bi « 1). Heat couplings between between the different thermal masses are defined through the heat resistance which was defined in equations 19, 20. The thermal system can be represented by a lumped electrical model. In order to maximize heating efficiency the heat resistance to the propellant must be minimized while maximizing the heat resistance to the bulk silicon and to the surrounding environment. To optimize the response time the thermal mass of the micro-heater must be minimized which can be achieved by removing bulk silicon and and maximizing the lateral heat resistance to the surrounding silicon. In addition the time constant of the temperature response during operation of the thruster is dependent on the thermal contact to the propellant. For heater of volume V being cooled through forced convection on a surface area A the time response is usually modelled as

$$\tau = \frac{pc_p V}{hA} \tag{30}$$

.

2.2 Design overview

The proposed heating chamber design does not include an internal channel structure. This is done to reduce pressure losses and simplify the instability behavior by eliminating the effects of parallel channel interactions and explosive boiling at the fin edges. Smooth channel walls are created that enable the delivery of uniform and high heat flux. Heating efficiency is improved by delivering heat from both top and bottom channel surfaces. Titanium heaters are integrated on glass with SiO_2 as a passivation layer. The top surface silicon heater is fabricated inside a recess bringing it closer to the desired channel height, minimizing conduction losses and heat capacitance. Thicker sections of silicon are placed between the recesses in order to maintain structural stability. The heat insulation provided by the thin silicon membrane and glass wafer enables non-uniform heat flux distribution along the length of the channel and step-wise heating. In this way the heat transfer can be optimized by delivering more heat closer to the inlet where heat transfer is more efficient. In addition pressure and vapor fraction measurements can be performed in-between recesses in order to evaluate heater performance. A 3D model of the proposed design is shown in figure 7.

Power loss due to friction losses which was given in 41 must be much lower compared to the Power needed to vaporize the flow. Larger diameter needed for lower friction loss. Channel diameter also affects heat transfer smaller diameter increases heat transfer up to a limit. A diameter of $200\mu m$ is chosen based on figure 41 since the friction factor increases rapidly below that value.

The thin membrane thickness results in better temperature coupling between heater and propellant. In addition the total thermal mass of the heater is reduced because of the removed silicon and because of the reduced thermal coupling to the surrounding substrate. The time constant of the temperature response is dependent on the total heated volume as shown in equation 30. The exact amount of thermal volume also depends on the thermal coupling to the surrounding substrate and needs to be calculated numerically. Finally, heat transfer and time response can be improved by removing silicon however this also affects the maximum flow rate/pressure in the micro-channel and consequently the maximum produced thrust of the thruster. This trade-off will be investigated using FEM simulations.

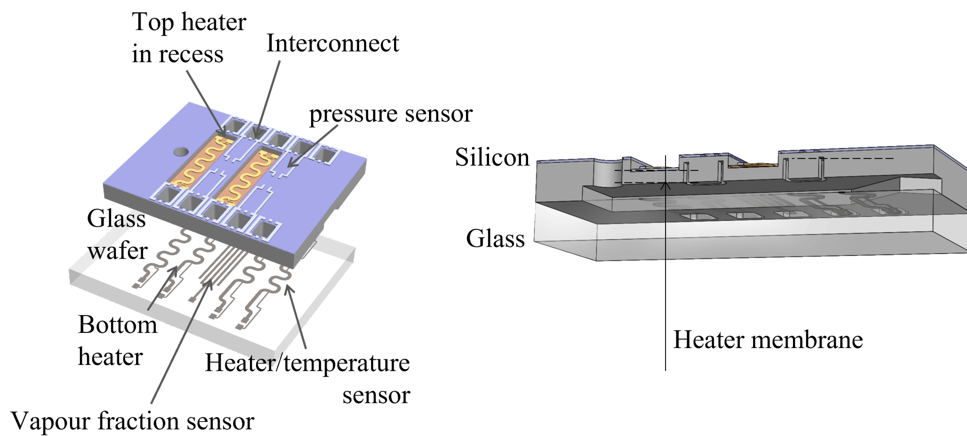

Figure 7: 3D model of proposed Design

2.3 FEM simulations

Heat transfer coupled with fluid dynamics and structural mechanics is simulated using the finite element method in COMSOL multiphysics. The purpose of the simulations is to:

- Evaluate the effect of the membrane thickness on the heating efficiency and transient response of the heater
- Compare the performance between single sided and double sided heat delivery.
- Compare the contribution of the different heat transfer modes
- Optimize the resistor geometry to improve Temperature uniformity
- Verify the mechanical stability of the structure

Phase transition and two phase flow is not included in the simulations as it is too complicated to model and requires too much processing power. Instead results are computed for single phase flow of either water or vapor.

2.3.1 Heat transfer simulations

The 3D model used in the simulation is shown in figure 8. The used modules for this simulation are "Heat transfer in solids and fluids", "Laminar flow" and "non-isothermal flow".

The laminar flow interface is used to compute the velocity and pressure fields assuming a low Reynolds's number for the micro-channel. The "weakly compressible flow" option is selected for the physics model which means that fluid density is dependent on temperature but not on pressure. The boundary conditions that need to be specified for this interface are the mass flow rate at the inflow and the pressure at the outflow. The internal channel channel walls are defined by a no slip boundary conditions which imposes a velocity of zero for the fluid flow on the wall surface.

The upstream temperature of the inflow is 293 K for water flow and 373 K for vapor flow. Convective heat flux to air as described by equation 16 with a transfer coefficient of 5 $W/(mK)$ and radiation to ambient as described by equation 17 is applied on the external walls. Convective heat flux to the fluid is present on the internal channel walls. The heat transfer coefficient is calculated by COMSOL through the multiphysics coupling between heat transfer and laminar flow.

2.3.1.1 Membrane thickness

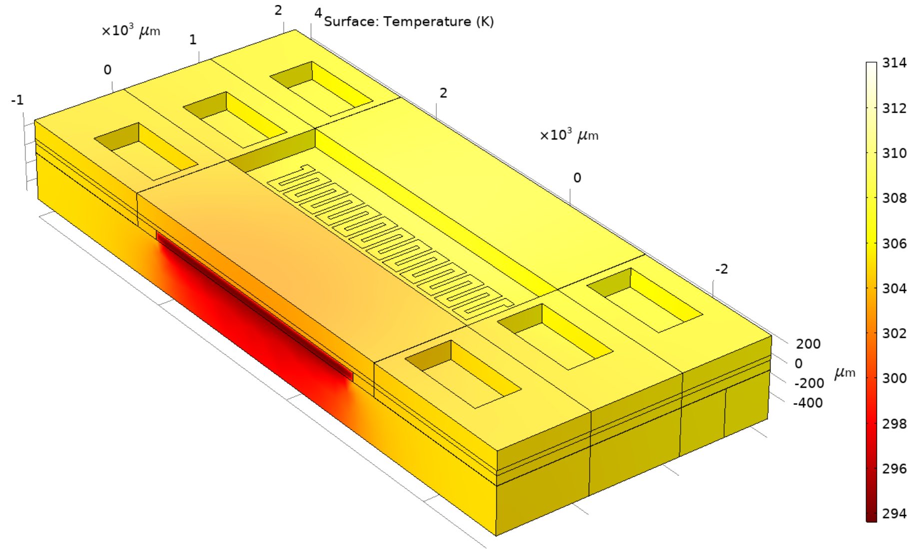

Figure 8: 3D model used in simulation

The results of the simulation are interpreted using the electrical model analogy as defined in 18, 27. The thermal resistance between the heater and the propellant is calculated in steady state condition using :

$$R_{fluid} = \frac{T_{surface} - T_{fluid}}{P_{fluid}} \tag{31}$$

Where P_{fluid} is the power transferred to the fluid. Similarly the thermal resistance to ambient can be defined as:

$$R_{ambient} = \frac{T_{surface} - T_{ambient}}{P_{ambient}} \tag{32}$$

where $P_{ambient}$ is the power lost to the surrounding environment . The temperature of the fluid T_{fluid} is obtained by integrating over the cross-section at the outflow. The temperature of the top silicon surface $T_{surface}$ is obtained by integrating over the heater membrane. The normalized heat resistance for different membrane thickness for single and double sided heating are shown in figure 9. As can be observed from the figure heating efficiency is enhanced by evenly distributing the power between the silicon and glass heater. The isothermal contours for the two configurations are shown in figure 10. Because glass has very low heat conductivity heating uniformity is significantly improved by applying power from both sides.

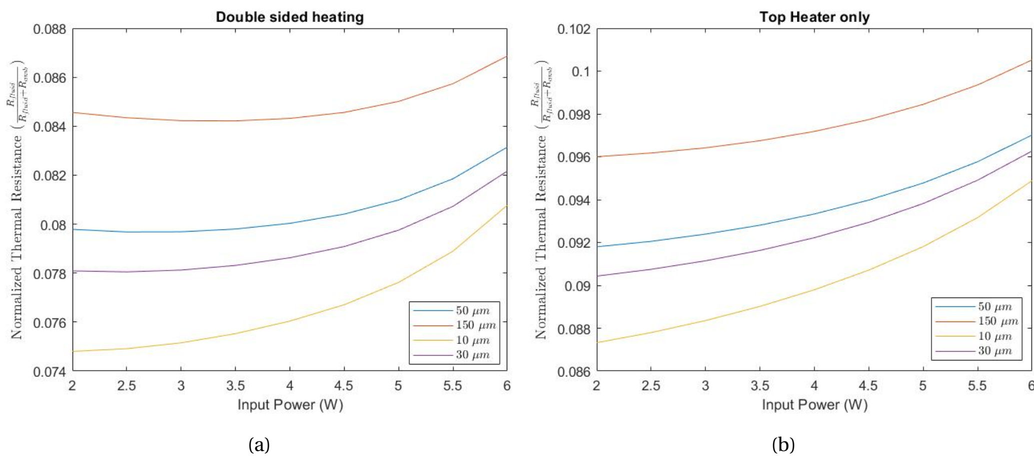

(a)

(b)

Figure 9: Normalized thermal resistance to the flow for single sided and double sided heating

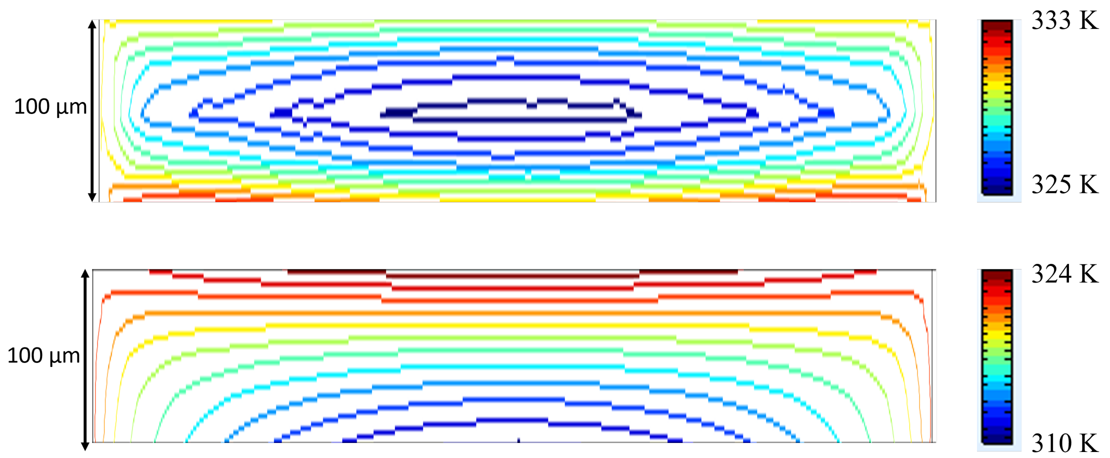

Figure 10: Isothermal contours for single(bottom) and double sided(top) heating

The transient temperature behaviour is computed by running a "time dependent" study. Results are shown in figure 11. By reducing the thickness of the silicon membrane the total thermal mass of the heater becomes lower while increasing the heat transfer to the fluid. This leads to an almost quadratic reduction in the time constant of the temperature response. The thermal capacitance with respect to the membrane thickness is shown on figure 12

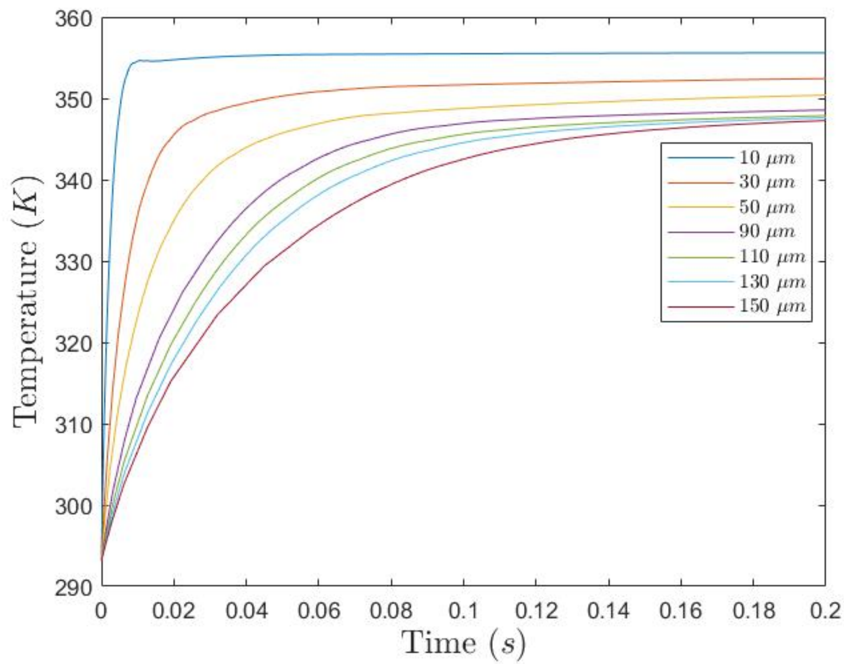

Figure 11: Thermal capacitance of top silicon heater as a function of the membrane thickness

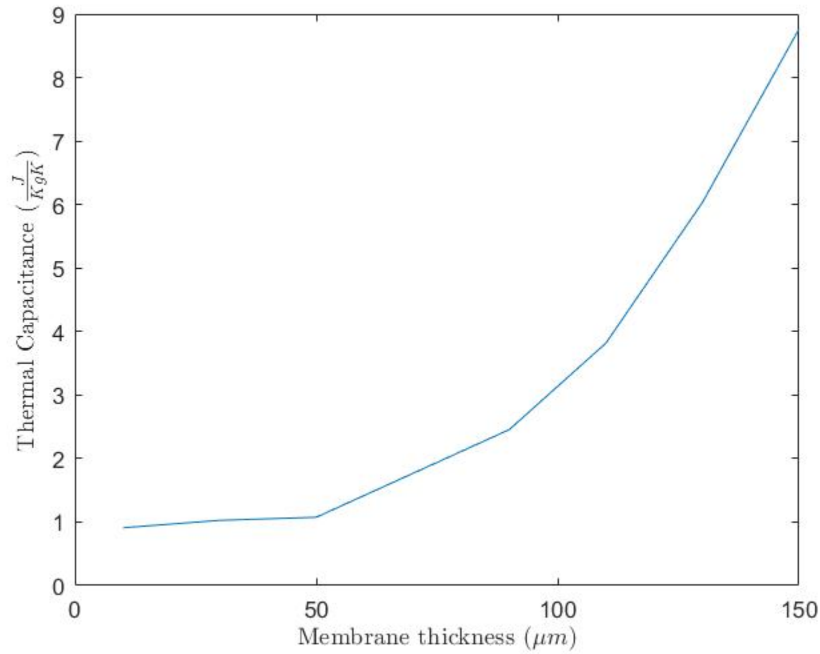

Figure 12: Thermal capacitance of the heater as a function of the membrane thickness

2.3.2 Mechanical simulations

Silicon can be removed to increase the thermal performance of the vaporization chamber as long as the structure is sufficiently strong. The maximum pressure that the structure must be able to withstand is set at 5 bar. This is the value used in previous designs that were integrated with the same nozzle. Although, in the current design the fluidic resistance is lower and therefore the pressure required to supply the same flow is expected to be lower.

In this section the mechanical stability of the silicon membrane and the titanium resistive heaters is evaluated. The stress inside the resistive layer caused by thermal expansion and membrane deflection is computed to verify that it does not exceed the maximum tensile stress of titanium. For this simulation the modules "heat transfer in solids", "solid mechanics" and "electric currents" are used. The deflection and induced stress on the silicon membrane are computed using a linear model meaning that no plasticity effects are included and the Youngs modulus of the material remains constant regardless of its deformation. As a rule of thump this model can only be considered valid when the deflection is at least five times lower than the membrane thickness.

The thickness of the membrane is varied while applying a pressure of 5 bar. Figure 58a shows the displacement at the center of the silicon membrane. The maximum stress at the membrane edges is shown figure 58b. The lowest membrane thickness that can be simulated using the linear elastic model is approximately 25 μm. Considering a 100 μm channel the maximum membrane displacement should be below 1 μm in order to minimize the effect on the flow. Another variable that needs to be considered is the effect on the heater resistance. The sensitivity of the resistance with respect to the chamber pressure must be as low as possible since the heater module is also used as an RTD. The resistance change for different membrane thicknesses is shown in figure 59. It is observed that the resistance with respect to pressure is negligible for all membrane thicknesses this is partially due to the meandering shape of the heater. Based on the results the selected membrane thickness is 30 μm

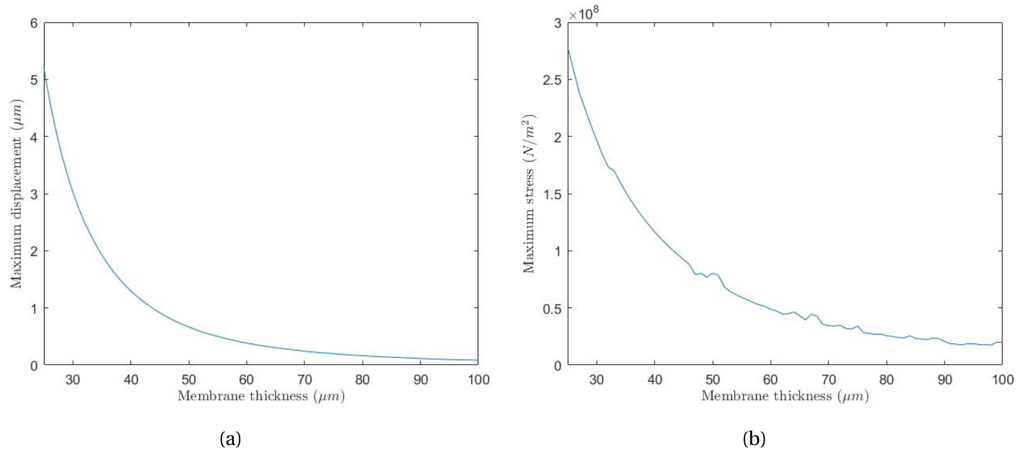

Figure 13: a)Maximum membrane displacement at 5 bar b)Maximum induced stress on top membrane surface at 5bar

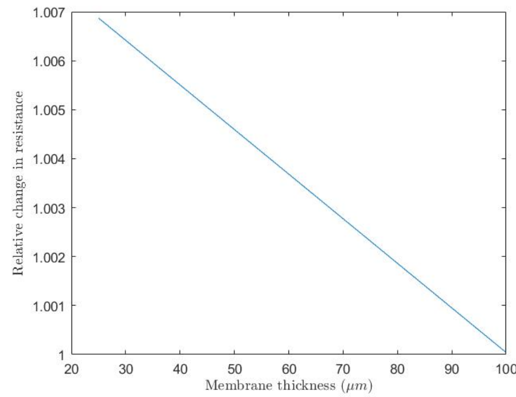

Figure 14: a)Maximum induced stress as function of input voltage b)Deflection caused by thermal expansion

2.3.2.1 Uniformity optimization

The pitch and width of the lines is optimized through FEM simulations in order to maximize temperature uniformity along the width of the channel. The pitch and width follows an exponential settling function along the channel width defined as:

$$w(n) = w_0 + a(1 - e^{bn}) \tag{33}$$

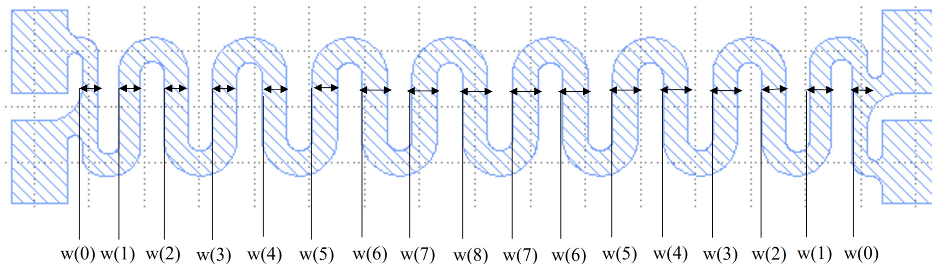

The achieved temperature uniformity is evaluated for heaters with different values of a and b. The total number of straight line segments is fixed at 18. The pitch and width of the line segment at the edge w_0 is adjusted so that the total area of the heater remains constant. The minimum value of w_0 is determined by the maximum total resistance specification, the required

mechanical strength and fabrication constraints. As the distance increases from the edge of the membrane the pitch and width of the straight line segments exponentially settles to $w_0 + a$ at the center. The temperature distribution on a $30\mu m$ silicon membrane for different resistor geometries is shown in figure 15 . The temperature distribution is largely influenced by the substrate material and thickness .Silicon acts as a heat spreader and thicker silicon membranes require a smaller variation in pitch and width to achieve the same temperature uniformity. Glass has a very low thermal conductivity and therefore the line-width relative to the pitch must be much higher. Furthermore, the structures on glass are capped with anodic bonding and therefore must be as thin as possible to achieve strong adhesion and leak-free wafer bonding. Hence the resistor must be wider to achieve the same resistance as the on-silicon resistor.

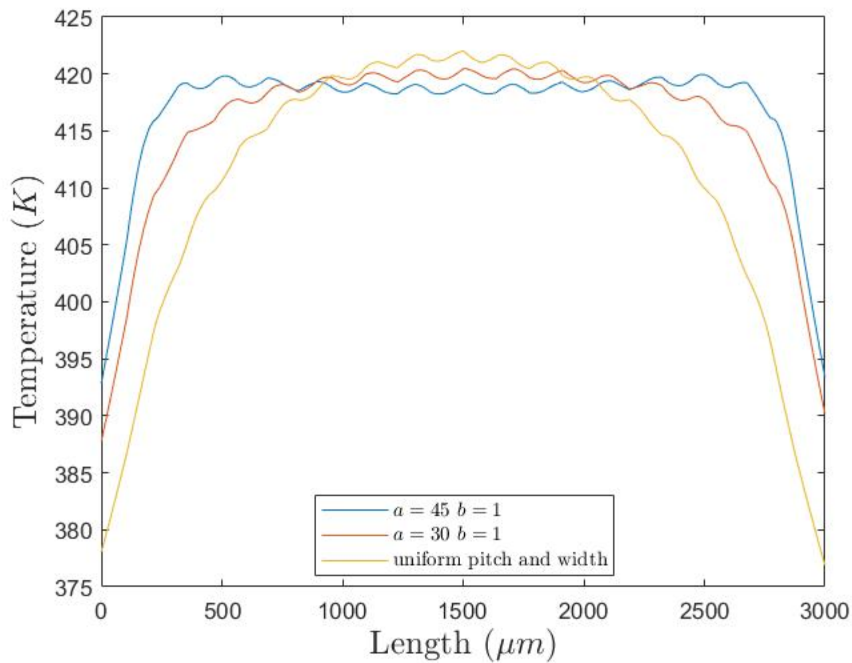

Figure 15: Temperature distribution on the silicon heater for different resistor designs

2.4 Conclusion

In this chapter the design of the vaporization chamber was presented. The proposed design was validated through FEM simulations. Due to limitations in computational resources a complete numerical evaluation of the thermal performance of the heater in two phase flow was not realized. However the simulations performed using the simplified single phase laminar flow model are sufficient to qualitatively assess the effects of different geometric parameters on the temperature distribution, heating efficiency and mechanical stability. Integrating an additional microheater on the glass surface to implement double increases the heating efficiency by approximately 20%. Removing silicon from underneath the on-silicon microheater reduces the heat resistance to the propellant as well as the relative loss to the surrounding environment. The power required for a single heater module to fully vaporize a given flow rate could not be derived from the simulations however because of the modular design approach the total channel length is variable. Vaporization chambers with different lengths can be placed on the wafer and experimentally determine which ones meets the required performance criteria. One of the main advantages of the proposed heater design is that the height of the fluidic channel can be tuned without influencing the energy losses caused by heat conduction. This allows the experimentation with more types of micro-fluid channel designs. In addition the variable channel height significantly simplifies the design of the planar vapor fraction sensor which will be presented in the next chapter.

3 Vapor fraction sensor

Vapor fraction measurements provide information about heater performance. The vapor fraction and its temporal, spatial variations are a characteristic of the flow regime. Previous research has shown that the capacitive sensing principle can be employed to determine the void fraction. The capacitance of the channel is a function of the material properties (electrical permittivity of the two phases), the void fraction and the flow regime. However, the majority of the literature concentrates on mini-channels with characteristic diameters ranging from 1-3 mm to a few centimeters and generally employing concave or helical electrodes [31]. Very few research is done on capacitive sensors for integrated micro-channels. In [32] a capacitor with a parallel plate structure is used to measure the void-fraction in parallel micro-channels. In this project the sensor must be integrated in parallel with a heater or pressure sensor. For this reason a planar capacitor is needed that allows single sided access into the channel.

3.1 Theory and design

3.1.1 Capacitance

The measuring principle of capacitive sensors is based on the interaction of a monitored medium and an applied electric field between the sensor electrodes. Since the electric field penetrates through the medium, electric displacement is generated inside it, which alters the charge stored between the sensor electrodes. The amount of stored charge is proportional to the capacitance seen by the two electrodes which is given by

$$C = \frac{\epsilon_r \epsilon_0 A}{d} + \frac{2\pi\epsilon_r\epsilon_0}{log(d/t)} \tag{34}$$

where ϵ_r is the relative permittivity of the monitored medium, A is the area of the electrodes d is the distance between them and t is the electrode thickness. For a parallel plate configuration where the dimensions of the electrode surface are much larger than its thickness the second term in equation 34 which is known as the fringe capacitance can be neglected. Whereas for a planar capacitor the fringe capacitance becomes dominant. For a planar capacitor the fringe field penetrates into the medium allowing single sided access. The penetration depth of the electric field is proportional to distance between the center-lines of the two electrodes. To maximize the effect of the fringing fields in the total capacitance a structure with interdigitated fingers can be designed as shown in figure 16. Capacitance derived from different finger pairs are connected in parallel. Therefore the total capacitance is a summation of capacitance contributed by neighbouring fingers. An approximation of the total capacitance for a semi infinite single layer medium is given by

$$C_f = (N-3)\frac{C_I}{2} + 2\frac{C_I C_E}{C_I + C_E} \tag{35}$$

Where N is the number of electrodes. C_I is half the capacitance of one interior electrode relative to the ground potential and C_E the capacitance of one outer electrode relative to the ground plane next to it.

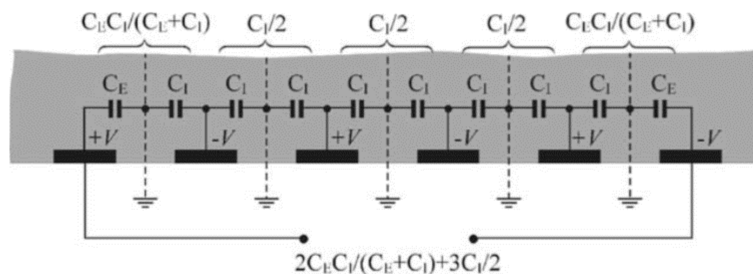

Figure 16: Capacitance of interdigital electrodes

3.1.2 Dielectric permitivity of water

Figure 17 shows the dielectric constant of water as a function of temperature and pressure. As temperature increases a sharp drop in dielectric constant is observed which corresponds to the phase change from liquid water to vapor. The dielectric constant of vapor is much lower compared to that of water. Therefore a larger fraction of vapor will result in lower average dielectric constant and lower capacitance. However the measured capacitance is not only a function of the volumetric vapor fraction but also the vapor distribution inside the channel. In the case of bubbly flow the alignment between the bubble pattern and the electric field will affect the electric field as seen by each bubble [33]. Without prior knowledge of the flow regime the void fraction can not be determined from a capacitance measurement. A solution to this problem is to assume a certain void pattern and calibrate the sensor accordingly. The void pattern is characterized by the average bubble size and the bubble distribution. For a boiling process in the microchannel the average bubble diameter is quite often close or larger than the hydraulic diameter of the channel.

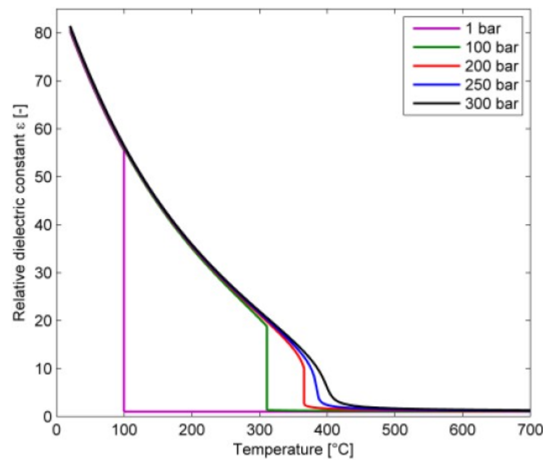

Figure 17: Dielectric permittivity of water as function of pressure and temperature [34]

In the case of bubbly flow the way in which the bubbles are 'aligned' with the electric field will also influence the capacitance. The bubbles can be homogeneously distributed throughout the volume of space or they could be aligned perpendicular or parallel to the electric field, Figure 2.1 illustrates this idea:

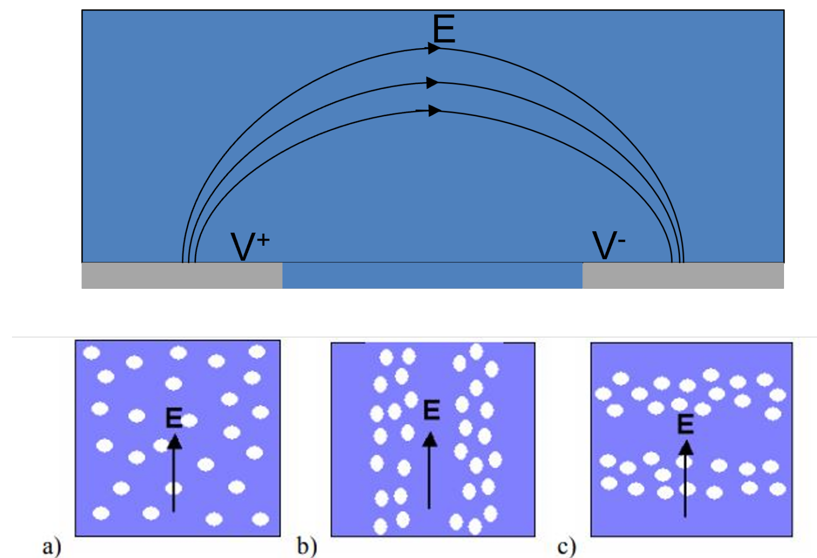

Figure 18: a) uniform distribution b) parallel distribution c) perpendicular distribution

In the parallel case the bubbles can be modeled as capacitance connected in parallel, while in

the perpendicular case as capacitors connected in series. For the parallel case the total effective dielectric constant is given by:

$$e_{eff} = \frac{e_r}{e_r a + (1-a)} \tag{36}$$

and in the perpendicular case by:

$$e_{eff} = a + (1-a)e_r \tag{37}$$

In conclusion, even in the presence of perfectly uniform electric field non-linearities in the measured signal are caused by the effect of bubble distribution. The magnitude of the error increases with larger sensing area and larger spatial wavelength in the case of interdigital capacitors. In addition, the dielectric constant of liquid water is a strong function of temperature and the vaporization temperature increases with increasing pressure, therefore the accurate determination of the vapor fraction is difficult without information about the vapor distribution, temperature and pressure.

3.1.3 Inter-digital capacitor design

The signal strength of the inter-digital capacitor can be optimized by tuning the sensing area the number of a fingers and the distance between them. The penetration depth of the fringing fields inside the channel is directly proportional to the spatial wavelength which is defined as

$$\lambda = 2(w + d) \tag{38}$$

where w is the width of one finger and d the distance between adjacent fingers. The signal strength is also dependent on the material parameters of the substrate. A substrate with a higher dielectric constant leads to more of the capacitors energy being stored in the substrate and lower signal amplitude. Therefore, sensor performance can be en chanced by choosing a substrate with low dielectric constant or by placing a grounded metal plate below the sensor that prevents the electric field from penetrating into the substrate .The total area of the sensor is fixed to $3mm$ by $1mm$ which is module size for this design. When the entire channel volume is to be probed an important parameter that needs to be considered is the uniformity of the electric field. If the electric field is uniform a vapor bubble would result in the same change in capacitance regardless of its position inside the channel. The sensor geometry is optimized through finite element method (FEM) simulations in COMSOL Multiphysics. The goal of the simulations is to investigate the electric field distribution and penetration depth for different sensor geometries. and to minimize the base capacitance(capacitance when no vapor is present) and maximize the dynamic range while maintaining sufficient probe depth.

3.1.4 FEM simulations

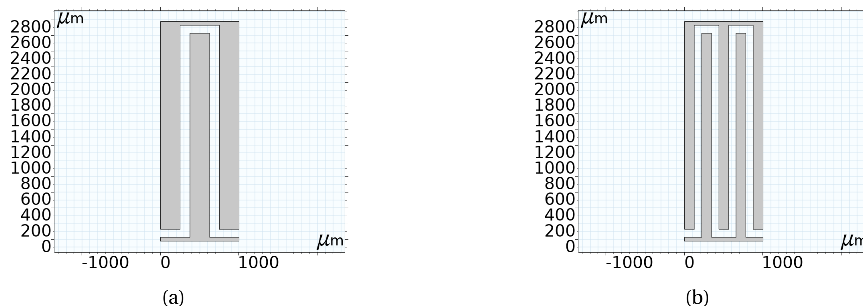

Figure 19: a) n=1 b)n=2

In this simulation materials are only defined by their relative dielectric permittivity. Materials used are borosilicate glass($\epsilon_r = 3$), silicon oxide($\epsilon_r = 3.9$) water vapor ($\epsilon_r = 1$) and water ($\epsilon_r = 55$). The relative permittivity of water is a strong function of temperature and pressure. Since the heating of water is not simulated in this stationary simulation. The water is assumed to be uniformly heated at $100C\hat{o}$ at atmospheric pressure which corresponds to a relative dielectric permittivity of 55. The geometry used in simulations is shown in figure. Because the width of the electrodes is

much larger than the height, the parallel plate capacitance is considered negligible and the sensor electrodes are modelled as two dimensional voltage terminals on the surface of the $500\mu m$ thick layer of borosilicate glass covered by a thin layer of SiO_2. The 100 μm channel consist of the water and vapor domain. The silicon layer (150 μm) is placed on top of the channel followed by vacuum. The vapor fraction is varied in three different ways. In one simulation the interface between the vapor and water domain moves vertically from the silicon surface towards the glass. The second simulation is made to simulate bubble elongation, the vapor-water interface moves horizontally. Finally, in the third simulation the channel volume is represented by one domain and its dielectric constant is varied between 1 and 55. Sensor performance is evaluated by running stationary electrostatic simulations for different vapor fraction values and calculating the capacitance.

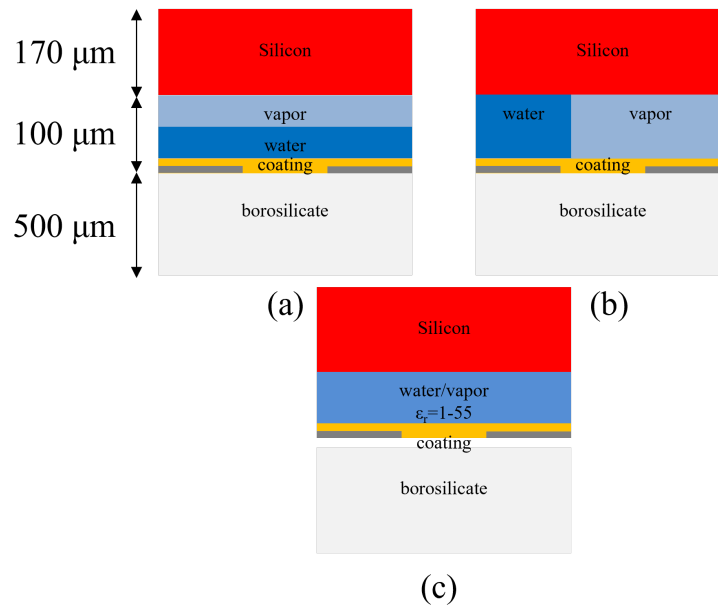

Figure 20: Different methods of varying the vapor fraction in simulations used in simulations

The first parameter to be investigated is the number of fingers n. Figure 19 shows the interdigital capacitor structure with a single finger. The capacitor consists of a single T shaped electrode on which voltage is applied and a grounded U shaped electrode. Figures show the capacitor structure for different numbers of fingers the total capacitor area is fixed to $1mm$ by $3mm$ so as the number of fingers increases the spatial wavelength λ decreases. Increasing n results in shorter distance between adjacent electrodes and consequently higher capacitance and lower penetration depth of the electric field. Figure 21 shows a visualization of the electric field for capacitors with 1 and 12 fingers. The penetration depth for each structure is obtained by incrementally increasing the thickness of the water layer until the capacitance reaches 97% of its value in saturation

$$\frac{C_p - C(tm = 0)}{C(t_m = \infty) - C(t_m = 0)} = 97\% \tag{39}$$

Where C_p is the capacitance when the thickness of the water layer is equal to the penetration depth, $C(t_m = \infty)$ is the capacitance when the water layer extends much further than the penetration depth and $C(t_m = 0)$ is the capacitance in the absence of water.

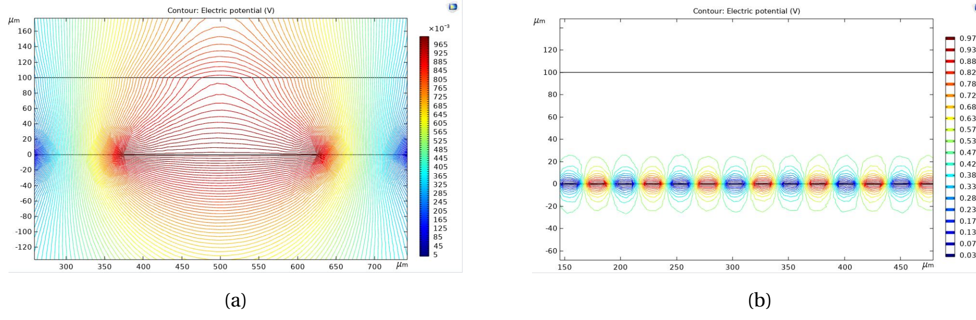

(a) (b)

Figure 21: Voltage contours a) n=1 b)n=12

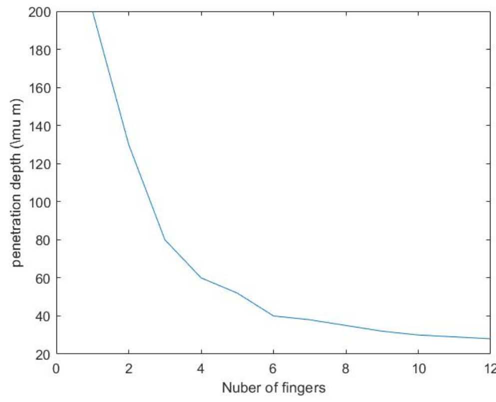

Figure 22: Penetration depth as a function of the number of fingers

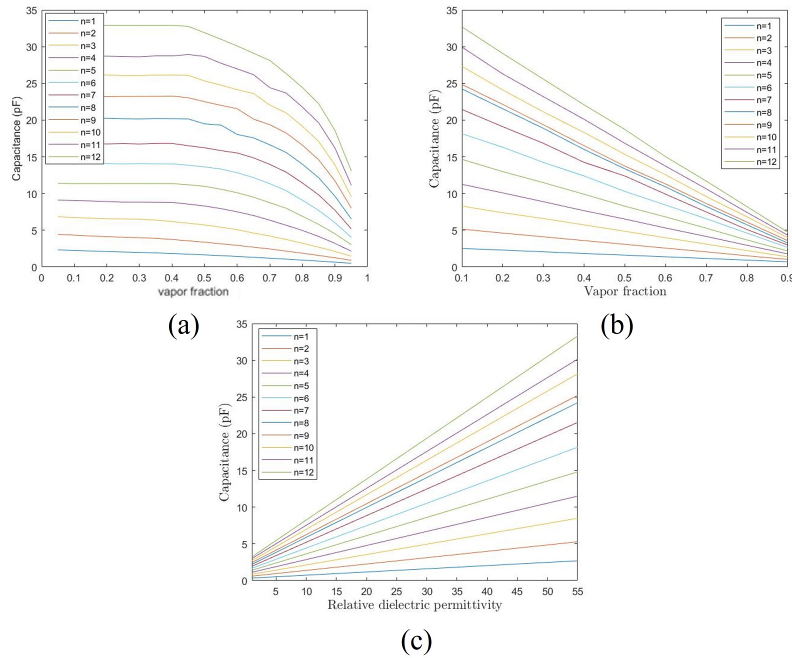

(a) (b)

(c)

Figure 23: Capacitive response to change in vapor fraction for different number of fingers

Figure 23 shows the capacitive response of the sensor to varying vapor fraction. Figure 22 shows the penetration depth as defined by equation 39 with respect to the number of fingers. When n is 3 the penetration depth becomes equal to the channel height. However the capacitive response to a changes in the vertical direction (figure 23)a) is highly non-linear. Linearity

depends on the uniformity of the electric field, a lower value of n must be chosen if a linear response is required. Furthermore, as mentioned earlier for maximum SNR the base capacitance must be minimized while maximizing the dynamic range. Increasing the number of fingers results in higher base capacitance but also sharper response. For $n = 10$ an optimal trade-off is achieved that maximizes SNR. However, the penetration depth for this value of n is only around $20\mu m$, nevertheless this design could still prove to be useful since for a thin high aspect ratio micro-channel the bubble diameter will reach the channel height very quickly and begin elongating. The error caused by the non-uniformity of the electric field can be evaluated by comparing the volumetric sweep of the of the vapor layer (figure 23)a,b) to the capacitive response of the material sweep (figure 23)c). The accuracy of the vapor measurement for each design can be evaluated by comparing the capacitive response to the two types of bubble growth to the response to a change in the average dielectric constant of the measured medium. The simulation results corresponding to the configuration of figure 23)b closely match those of figure 23)c meaning that the size of an elongated bubble can be measured accurately for all values of n. Regarding bubbles with diameters smaller than the channel height a capacitor with $n = 1$ can be employed to measure the void fraction with a relative error of approximately .1%.

Another parameter that needs to be considered is the finger width or the ratio between the finger width and the spatial wavelength. The variable r is used to calculate the width with respect to the number of fingers and the sensor area.

$$w = r\frac{lc}{n} \tag{40}$$

Increasing r results in increased sensitivity due to the broader electrodes moving together. As is observed in figure 24 the dynamic range signifficantly increases. Since the increase in base capacitance is smaller in comparison the SNR is improved.

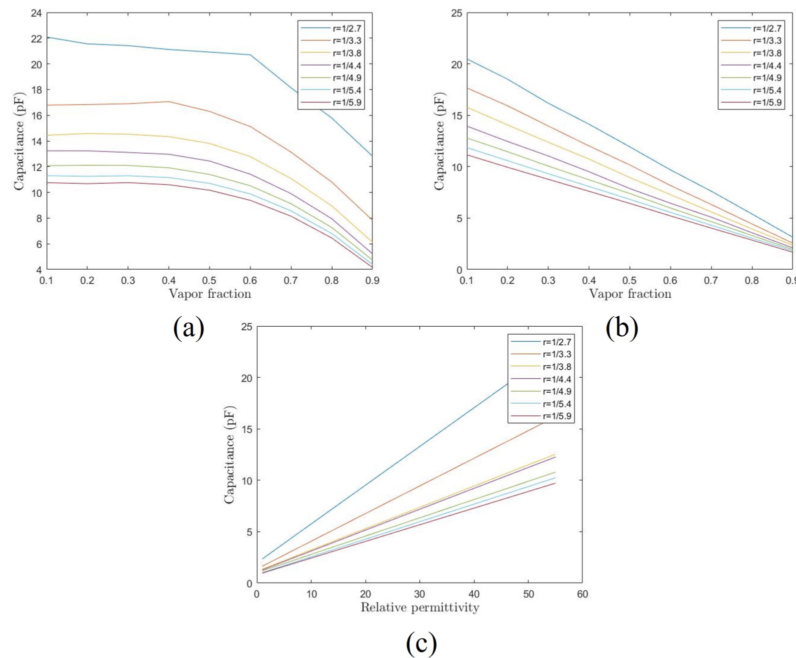

Figure 24: Capacitive response to change in vapor fraction evaluated for capacitors with different values of r

Another possible method to improve performance is to implement a three trerminal capacitor with a grounded plane placed below the electrodes that shields the sensor from noise while also improving the signal strength by eliminating the electrical energy that is stored in the glass substrate.

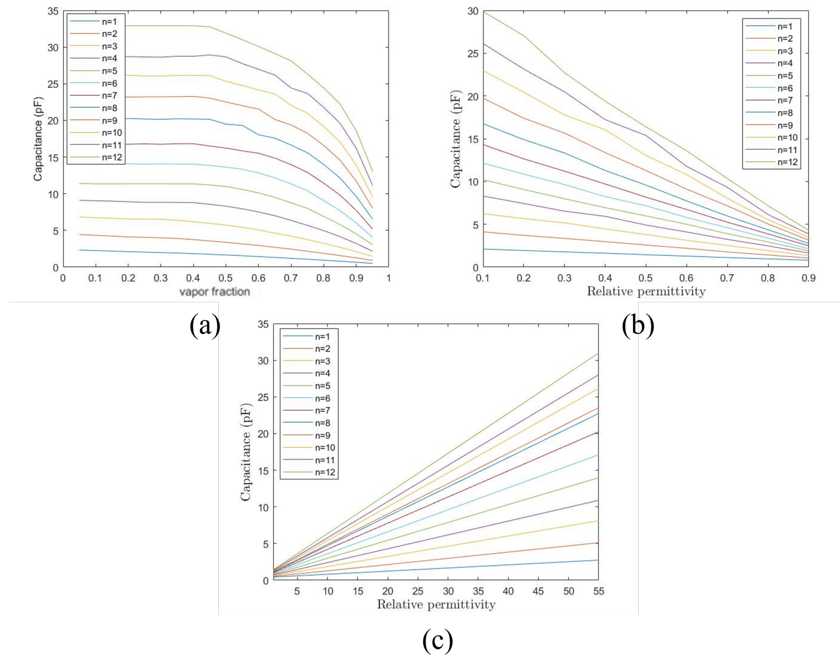

Figure 25: Capacitive response to change in vapor fraction of a grounded capacitor with $n = 10$

. In order to evaluate the effect of the back-plane, the simulations are repeated with the same settings. Results (figure 25) show that the grounding the capacitor reduces base capacitance while increasing the dynamic range. However this is only a minor improvement of about 3% since the dielectric constant of borosilicate glass is much lower compared that of water. Therefore the electric energy wasted in the glass substrate is much lower in comparison. Furthermore the thickness of the glass substrate is much larger than the penetration depth of the electric field meaning that that the sensed volume is fully contained within the device and external interference should not be an issue. Considering the added fabrication process complexity (additional metal layer, insulation layer, and etching of openings) the ground plane will not be considered in further analysis.

A protective coating is required to prevent chemical reactions between the metal electrodes and the fluid. The effect of the thickness and the permittivity of a coating on top of the interdigitated electrode structure is evaluated. For this purpose, the coating thickness is varied from 0 to $5\mu m$. Additionally, the effect of the permittivity is studied by evaluating two different materials SiO2 and SiN. For the simulations, an electrode thickness of $100nm$ is assumed. Additionally, the back-plane is neglected. Results are presented for a capacitor with 10 fingers.

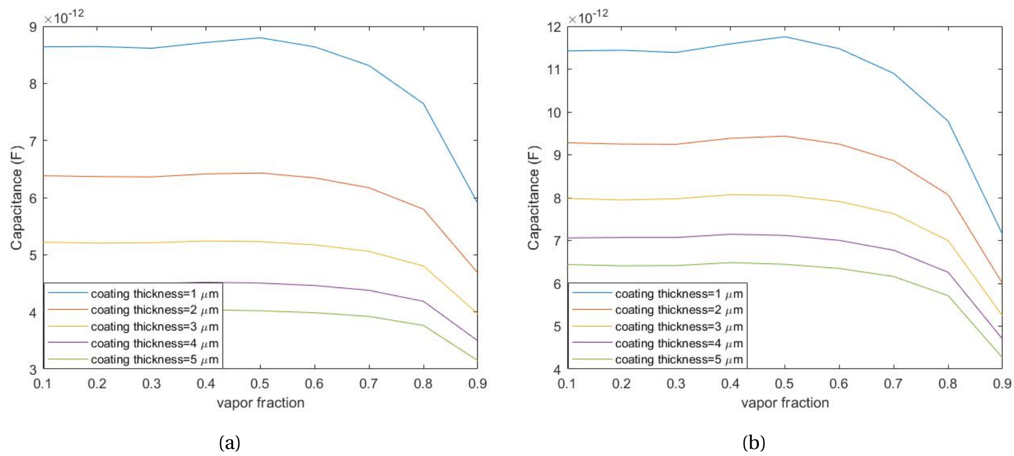

Figure 26: Capacitance as function of vapor fraction for different coating thicknesses

As the figure shows, the capacitance is damped increasingly with the coating thickness. Up

to a certain coating layer thickness, the behavior the capacitance curves shows is a similar exponential behavior as before. However, as coating thickness approaches the penetration depth of the electric field the the curve becomes flatter.

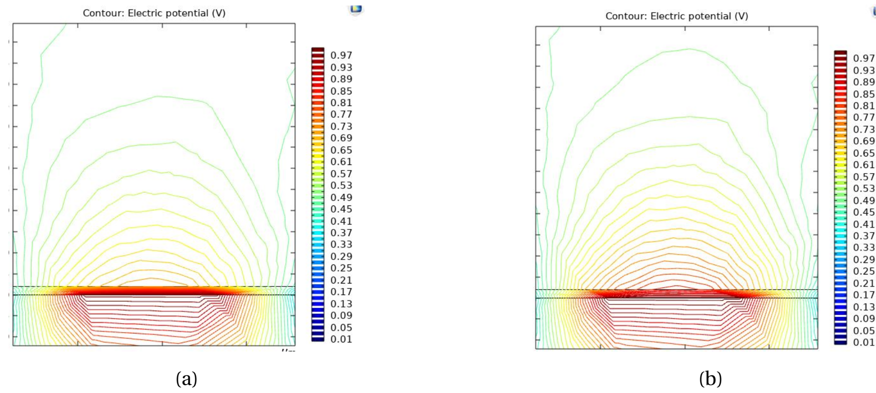

Figure 27: a) Voltage contours with a SiO_2 coating of $2\mu m$ b)Voltage contours with a Si_3N_4 coating of $2\mu m$

Figure 27 illustrates the electric field line and potential distribution for a coating thickness of 2 μm. In contrast to the behavior in figure 21, where no coating is applied, the electric field intensity inside the coating layer is significantly higher compared to the channel. Therefore for a large number of fingers a significant percentage of the total electric energy will be stored in the coating. This effect becomes more significant when a material with a higher dielectric constant is used like silicon nitride as shown in figure . Thin layers are also required in view of process compatibility with anodic bonding. For integration the glass surface should be as flat as possible.

3.2 Conclusion

A capacitive vapor sensor with an inter-digital electrode structure was designed and optimized through FEM simulations. The simulations showed a trade-off between sensitivity and vertical probe depth. Based on those results two different sensor designs are integrated in the microthruster that achieve opposite ends of the trade-off:

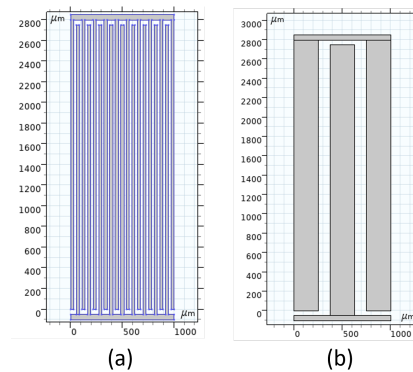

Figure 28: Integrated capacitor designs

The capacitor of figure 28b with a base capacitance of 1.5pF and a dynamic range of 1pF creates an electric field that is mostly uniform inside the channel and is able to sense the volumetric vapor fraction of the entire volume. The design of figure 28a has a base capacitance of 20 pF and a dynamic range of 15pF but can only detect changes close to its surface. The larger penetration depth of the first sensor enables more accurate determination of the vapor fraction on the other hand the measurement becomes more sensitive to changes in vapor distribution because of the larger spatial wavelegth of the electric field. Both structures are designed with finger width to spatial wavelength ratio of .6. Larger electrode width could offer improved performance

however it would also be beneficial to allow better visual access into the channel for sensor calibration. The metal is coated with a SiO_2 layer of 150 nm. The back-plane is neglected as the slight performance improvement it offers is not worth the additional process steps. From figure 23 it was observed that the capacitive response follows an exponential roll-off behaviour. The capacitance stays constant until vapor interface reaches the vertical probe depth of the sensor at which point the capacitance drops sharply. More advanced sensing can be performed by measuring the capacitance between a single biasing electrode and multiple sensing electrodes located at an increasing distance from the biasing electrode. Each measurement will have a different vertical probe depth by combining measurements from multiple sensing electrodes the vertical distribution of vapor can be accurately determined. Many similar methods of planar capacitive sensing have been reported in literature [35]. However since electrical connections to the internal structures are difficult to realize increasing the number of connections makes fabrication more complicated. For this reason, these advanced measuring methods will not investigated in this project however its worth noting that these planar capacitors can be used to determine not only the average vapor fraction of the entire channel volume but also its distribution inside the channel

4 Pressure sensor design

4.1 Pressure sensors

Knowledge of the pressure drop along the channel length as well as pressure oscillations is extremely important for the determination of the friction factor losses and the characterization of the flow. For this purpose pressure sensors are integrated within the vaporization chamber. In a previous work the holes were etched at various points across the vaporization and pressure was measured using a commercial pressure sensor which was attached adhesively. The inclusion of an integrated pressure sensor instead of an external one has the advantage of a lower added channel volume as well as increased robustness. The effect of the added channel volume on the accuracy of the measurement can be seen in equation 41 which shows the pressure drop caused by a change in cross-sectional area

$$\Delta p = K_L \frac{\rho u^2}{2} \tag{41}$$

where u is the average cross-sectional velocity and K_l is an empirically determined constant. Values of K_L for different channel geometries can be found in [36]. This function can effectively be used to compensate for the added volume assuming in-compressible liquid flow, however in the case of gas or two phase flow where the fluid density isn't precisely known the added volume of the pressure sensor can create significant error. Besides the added volume, important design considerations for an integrated pressure sensor are the temperature dependency and response time. Fast measurement time is required to measure the sharp pressure changes caused by explosive boiling phenomena and pressure drop instabilities. Low temperature dependency is needed as the VLM can reach very high temperatures in order to produce the required thrust output. Finally, the sensor is designed for a pressure range of 0-5 bar which is equal to the range of the feeding pressure.

Attributes	Piezoresistive	capacitive	Optical	Resonant	Force-balanced
Sensitivity	Good	Good	Excellent	Good	Fair
Dynamic Range	Good	Fair	Excellent	Good	Excellent
Size	Excellent	Excellent	Poor	Fair	Fair
Integratability	High	Medium	Low	Medium	Medium
Temperature dependency	High	Low	None	Medium	Medium
robustness	Fair	Good	Excellent	Fair	Poor
response time	Low	High	High	medium	Low

4.2 Membrane design

The most common types of pressure sensors are those that operate based on the deformation of a suspended membrane due to applied pressure. These include piezoresistive, piezoelectric, capacitive optical, force balancing and ponteciometric. For a rectangular membrane an approximate model of the deflection as a function of pressure is given by:

$$P = E\frac{h^4}{a^4}[g_1\frac{w_0}{h} + g_2(\frac{w_0}{h})^3] \tag{42}$$

Where P is the pressure load, a is the width of the membrane $w0$ the deflection at the center, H the membrane thickness, g_1 and g_2 are Poisson ratio v dependent constants given by:

$$g_1 = \frac{4.13}{(1-v^2)} \tag{43}$$

$$g_2 = \frac{1.98(1-0.585v)}{1-v} \tag{44}$$

For a circular diaphragm an exact solution exists for the deflection of the membrane which is given in polar coordinates by:

$$w(r) = \frac{Pa^4}{64D}[1-(\frac{r}{a})^2] \tag{45}$$

Where w,r,a are the displacement ,radial distance from the center and diaphragm radius respectively. D is the flexural rigidity, a material property given by:

$$D = \frac{Eh^3}{12(1-\nu^2)} \tag{46}$$

For small deflections, deflection can be considered directly proportional to the applied pressure, but that is not the case for large deflections or membranes with large built in stresses. Good linearity is generally desirable as linear sensors are easier to calibrate. When a linear deflection scheme is assumed the membrane can be modelled as a thin plate clamped at the edges. For a plate to be considered "thin" the ratio of thickness to length must be less than 1/20. In addition the maximum deflection must be small compared to the plate thickness. A rule of thumb that is commonly used for the design of pressure sensor membranes states that the maximum deflection must be less than 1/5 of the plate thickness. Another important consideration for membrane design is the burst pressure, which is defined the maximum pressure after which the membrane raptures. It has been suggested that the maximum applied pressure should be at least 5 times lower compared to the burst pressure [37].The burst pressure of a membrane is modelled as:

$$P_{burst} = \frac{3.4}{1-\nu^2}\frac{\sigma_{fracture}h^2}{A} \tag{47}$$

where $\sigma_{fracture}$ and A refer to the fracture stress and area of the membrane respectively. The burst pressure is also greatly affected by surface roughness. Smooth surfaces and rounded corners are required for a robust membrane [38]. In order to enhance the diaphragm's fracture strength, corner rounding using DRIE was proposed in [39].

A comparison of different pressure sensing mechanisms is shown in table 4.1. Piezoelectric sensors have high sensitivity, high temperature range and do not require an external power supply. However they are not suitable for static pressure measurements as the piezoelectric effect is only triggered during pressure changes. Optical fiber-based sensors as well as force-balanced and electromagnetic sensors have high sensitivity, high accuracy and no temperature dependence but have the disadvantage of high design complexity as they include multiple components and may require advanced circuitry or processing power. Piezoresistive and capacitive sensors are commonly used in many applications because of their small dimensions simple fabrication and compatibility with IC processes. Despite the very low temperature dependence of capacitive sensors, for application in VLMs piezoresistive sensing is preferred since low measurement time is required to detect the fast dynamic effects that occur inside the vaporization chamber.

4.3 Piezoresistor design

The relative change in resistance of a rectangular conductor is given by:

$$\frac{\Delta R}{R} = (1+2\nu)\epsilon + \frac{\Delta\rho}{\rho} \tag{48}$$

Equation 48 contains two terms. The first term is the change caused by changes in dimensions while the second term is the change due to piezo-resistive effect. For semiconductors like silicon the second term is considered dominant. The effect of stress on the resistivity of a crystalline material can be expressed by a 6x6 tensor with 36 independent coefficients which is referred to as the piezo-resistance coefficient matrix π. For silicon, due to the symmetric structure of the lattice this can be simplified to only have 3 independent components, resulting in the following relation

$$\begin{bmatrix}\Delta_1\\ \Delta_2\\ \Delta_3\\ \Delta_4\\ \Delta_5\\ \Delta_6\end{bmatrix} = \begin{bmatrix}\pi_{11} & \pi_{12} & \pi_{12} & 0 & 0 & 0\\ \pi_{12} & \pi_{11} & \pi_{12} & 0 & 0 & 0\\ \pi_{12} & \pi_{12} & \pi_{11} & 0 & 0 & 0\\ 0 & 0 & 0 & \pi_{44} & 0 & 0\\ 0 & 0 & 0 & 0 & \pi_{44} & 0\\ 0 & 0 & 0 & 0 & 0 & \pi_{44}\end{bmatrix}\begin{bmatrix}\sigma_1\\ \sigma_2\\ \sigma_3\\ \sigma_4\\ \sigma_5\\ \sigma_6\end{bmatrix} \tag{49}$$

	π_{11}	π_{12}	π_{44}
p-Si(7.8 $\Omega - cm$)	6.6	-1.1	138.1
n-Si(11.7 $\Omega - cm$)	-102.2	53.4	-13.6

P-type resistors are generally preferred over n-type due to their higher sensitivity.

4.4 Temperature compensation

The three main factors that contribute to the temperature dependency of piezo-resistive sensors are the Temperature coefficient of resistance TCR, the temperature coefficient of piezo-resistivity and thermal stress. The dependence on the TCR can be eliminated by placing resistors in a Wheatstone bridge configuration. The Wheatstone bridge consists of two voltage dividers each consisting of a parallel and a perpendicular resistor oriented 90 degrees apart with respect to the current flow resulting in opposite change in resistance. The output of the bridge is the differential voltage between the two voltage dividers which is given by equation 50 for a voltage driven bridge and equation 51 for a current driven bridge:

$$V_{out} = V^{+} - V^{-} = (\frac{R_2 R_3 - R_1 R_4}{(R_1 + R_3)(R_2 + R_4)})V \tag{50}$$

$$V_{out} = V^{+} - V^{-} = (\frac{R_2 R_3 - R_1 R_4}{(R_1 + R_2 + R_3 + R_4)})I \tag{51}$$

The Wheatstone bridge completely eliminates the effect of the TCR assuming uniform temperature distribution and perfectly matched resistors. However it also important to compensate for the temperature coefficient of piezo-resistivity $TC\pi$. The main factor that determines the $TC\pi$ is the doping concentration. In [41] a very useful equation was proposed that expresses the dependence of the piezo-resistive coefficient π_{44} with respect to temperature and doping concentration:

$$P(N_A, \theta) = \theta^{-.9}[1 = (\frac{N_A}{N_b})^{0}.43\theta^{-0.1} + (\frac{N_A}{N_c})^{1.6}\theta^{3}] \tag{52}$$

Where $\theta = \frac{T}{T_0}$, $T_0 = 300\ K$ and N_A is the doping concentration.

.The sensitivity of a pressure sensor with a constant voltage and current input is given by equations 53 and 54 respectively.

$$S_v = \frac{1}{\Delta P}\frac{1}{2}\pi_{44}\sigma_{eff} \tag{53}$$

$$S_i = \frac{R}{\Delta P}\frac{1}{2}\pi_{44}\sigma_{eff} \tag{54}$$

Where ΔP is the input pressure. The TCS can be expressed by :

$$TCS_v = \frac{1}{\pi} + \frac{1}{\sigma}\frac{d\sigma}{dT} \tag{55}$$

$$TCS_v = \frac{1}{\pi} + \frac{1}{R}\frac{dR}{dT} + \frac{1}{\sigma}\frac{d\sigma}{dT} \tag{56}$$

Where the last term represents the changes in stress due to temperature. From equations 56 it can be seen that in the current controlled case the TCS depends on both the TCR and the $TC\pi$. Since the TCR is a positive quantity and the $TC\pi$ is a negative quantity both effects can be compensated by choosing an appropriate doping concentration. A plot of TCR and $TC\pi$ for p-type resistors with respect to the doping concentration was shown in [40].The two curves intersect at two points. To maximize sensitivity the point with the lowest doping should be chosen which corresponds to a doping concentration of $10^{17}\ cm^{-3}$. Other methods of compensating for the $TC\pi$ that have been presented in literature include the use of external circuitry and the of the bridge resistors or additional piezoresistors for temperature measurements.

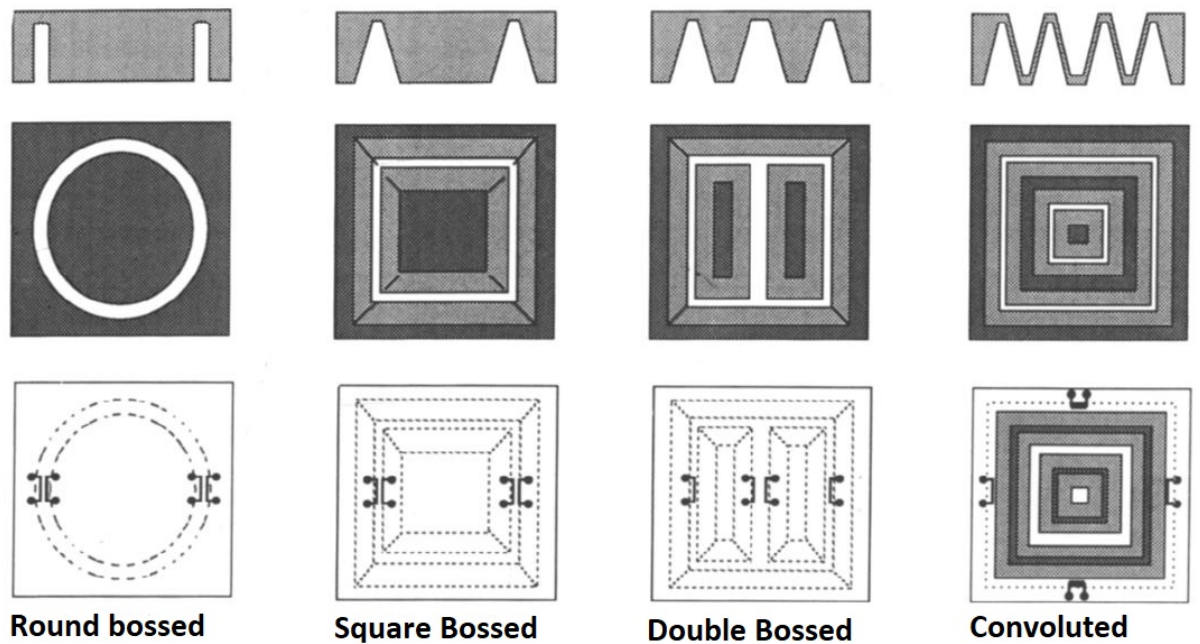

Figure 29: Low-pressure sensor geometries for enhanced linearity [44]

Temperature stress and its effect on the sensor output is mainly dependent on membrane geometry. When the membrane becomes thinner the temperature dependency of the offset voltage with respect to its output span values increases. Membranes with non-uniform thickness, often identified in literature as "bossed diaphragms" have been employed to circumvent this problem. Examples of bossed structures from literature are shown in figure 29. Local stiffening of the diaphragm is performed by adding thicker sections of silicon in areas where there are no piezo-resistors, which has the effect of higher stress for the same amount of deflection since the stress is concentrated in the piezo-resistor areas. For applications in two phase flow micro-channels these structures also have the advantage of higher measurement accuracy since most of the surface are of the membrane is brought to the same height as the channel.

4.5 Design overview

A piezo-resistive, bossed membrane pressure sensor is designed. To be compatible with the micro-thruster fabrication process, DRIE is used for the etching of the membrane. The total footprint of the sensor must fit within the module length of $1mm$. In these small dimensions the etch rate of the DRIE is significantly affected by the aspect ration of the crevices, therefore it is important that all crevices have the same width. For that reason double boss structures are excluded as a design choice as they require gaps of different widths. Integration of such structures would require wafers with a buried landing layer which are not available for this project. The proposed membrane design is a single boss membrane with rounded corners. The width of the boss and radius of the corners is optimized so that the stress on the inner and outer edge of the thin membrane is equal in magnitude.

P-type boron diffused resistors are formed in silicon through implantation. The implanted resistors have a doping concentration of 5e18 cm^{-3} which according to equation 52 achieves a good trade-off between temperature dependency and sensitivity. Four resistors are placed in a Wheatstone bridge configuration and an an additional resistor is placed in a zero stress region which acts as a temperature sensor. The temperature sensing resistor can be placed in an amplifier circuit that compensates for the $TC\pi$ by controlling the bridge voltage [40]. The dimensions and placement of the piezoresistors is determined from the stress profile, which is computed through FEM simulations.

4.6 FEM simulations

The stress profile and piezoresistive response is computed in COMSOL Multiphysics through the "structural mechanics" and electric "currents" modules. The mechanical stress and conductivity of the piezoresistors are coupled through equation 57

$$\sigma = \frac{\sigma_0}{1 - \pi_{44}\sigma_x} \tag{57}$$

Where σ_x is the component of the stress tensor that is perpendicular to the current flow. Assuming uniform doping concentration a two dimensional approximation is used for the calculation of the currents in order to save computational time. Pressure is applied on the bottom surface of the thin membrane and silicon boss. An important boundary condition that must be carefully considered is the "fixed constraint" condition which enforces a displacement of zero on the applied surface. Setting the "fixed constraint" on the sidewalls creates a stress profile which is contained within the area of the thin membrane, whereas when fixing the structure on the bottom surface the high stress region extents outside the outer membrane edge [43]. An appropriate meshing for the pressure sensor should be determined considering both efficient and accurate modeling. The thin film of the piezo-resistor has the finest mesh to model the stress field more accurately. The mesh becomes coarser away from this region as shown in 30.

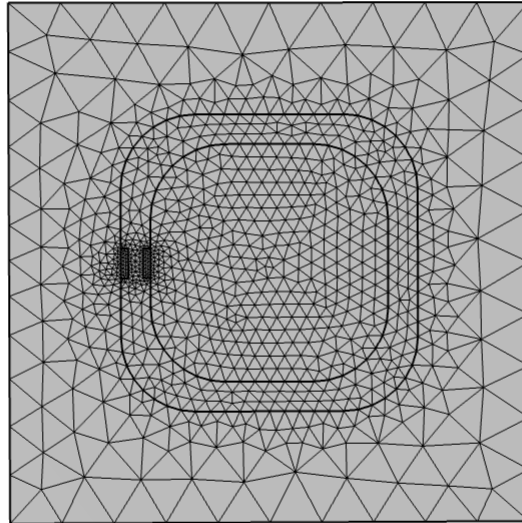

Figure 30: Topview of meshed geometry used in simulations

Figure 31 shows the transverse stress profiles for silicon boss structures with different diameters. The structure is clamped at the bottom. Firstly, the diameter of the silicon boss is varied in order to determine the minimum boss dimensions that result in stress of equal magnitude for the internal and external edges of the membrane. Pressure is applied at the bottom surface. The stress profile along the diaphragm for different boss diameters and and applied pressure of 5 bar is plotted in figure 31. The induced differential stress(difference of maximum tensile and compressive stress) with respect to the applied pressure is shown in figure 32b and the corresponding error caused by non-linearity as a percentage of the full scale values in figure 32a.

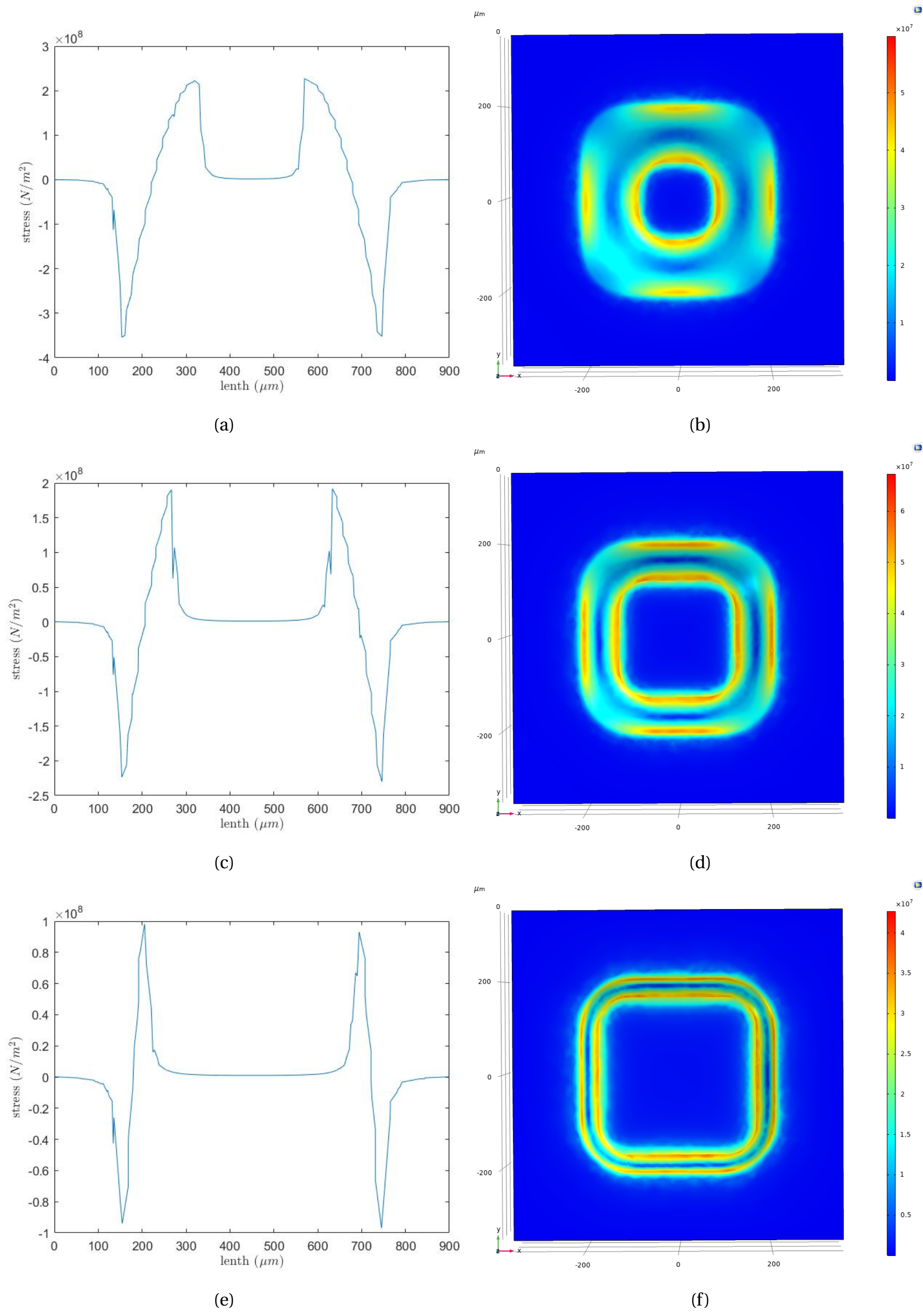

Figure 31: a)Non linearity as a function of Temperature for a single boss membrane b)Voltage output at different temperatures

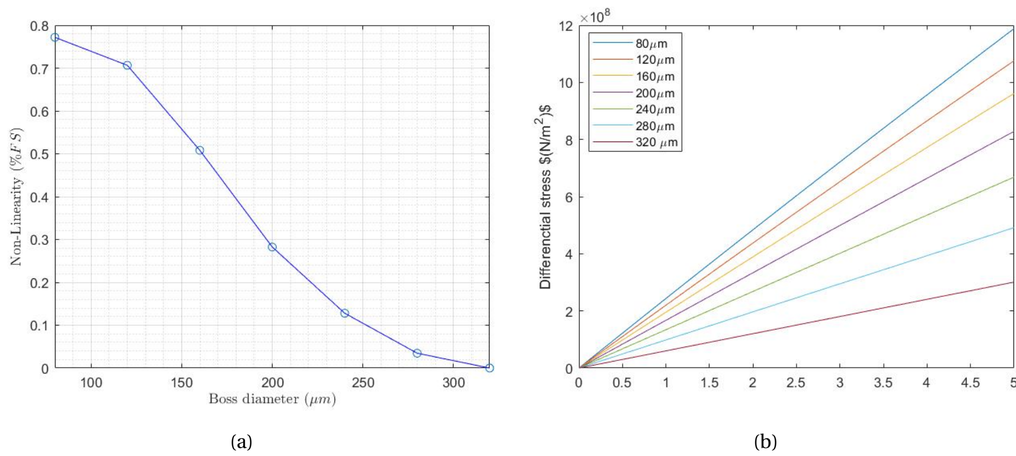

(a) (b)

Figure 32: Non-linearity for different boss diameters

When the silicon boss covers approximately 80% of the membrane area the compressive and tensile stresses at the diaphragm and boss edges become equal in magnitude resulting in optimal linearity. It is observed that the maximum stress on the membrane decreases as the rigid silicon boss becomes larger. However the induced displacement also decreases resulting in a more robust structure of the membrane (figure 36).

In figure 31 it is observed that the high stress region extends outside the membrane area, therefore the piezo-resistors need to be shifted by approximately 2 μm towards the membrane edges for optimal sensitivity. The piezo-resistors are designed to be 10μm wide and 70μm long which is enough to cover the entire stress region while also providing some robustness to fabrication tolerances. The simulated bridge output voltage is shown in figure 35b assuming a π_{44} coefficient of 0.8 at room temperature. The sensor has a full scale voltage output of 83 mV at a bridge voltage of 5 V

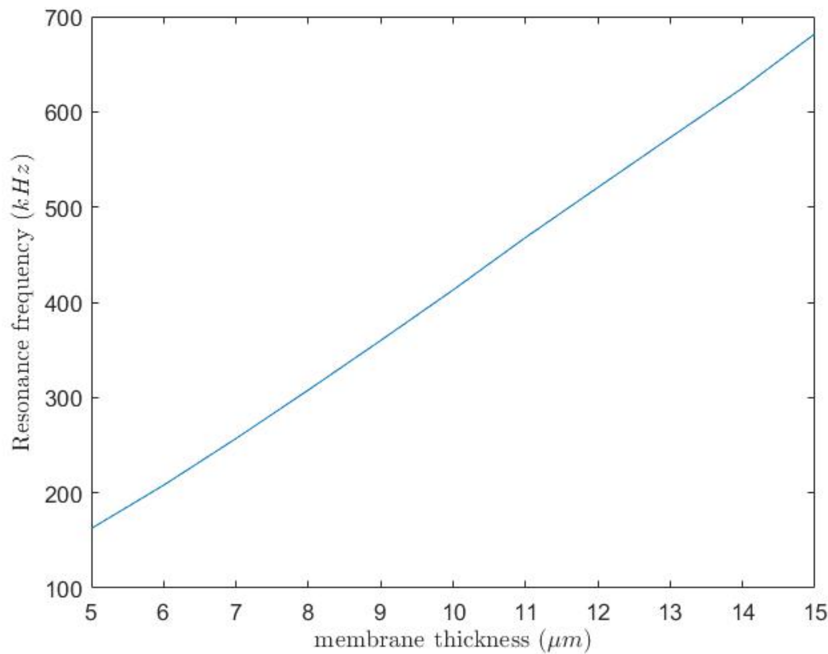

Figure 33: Resonance frequency with respect to membrane thickness

Eigen-frequency analysis was performed to determine the resonant frequency of the single boss membrane. The resonant frequency versus diaphragm thickness for thicknesses in the range of 5- 15 μm is given in figure 33, which shows the approximate linear increase in resonant fre-

quency with diaphragm thickness for a certain boss dimension. The resonance frequency ranges between 170MHz and 700MHz which corresponds to a settling time of 4.5ns to 1.2ns

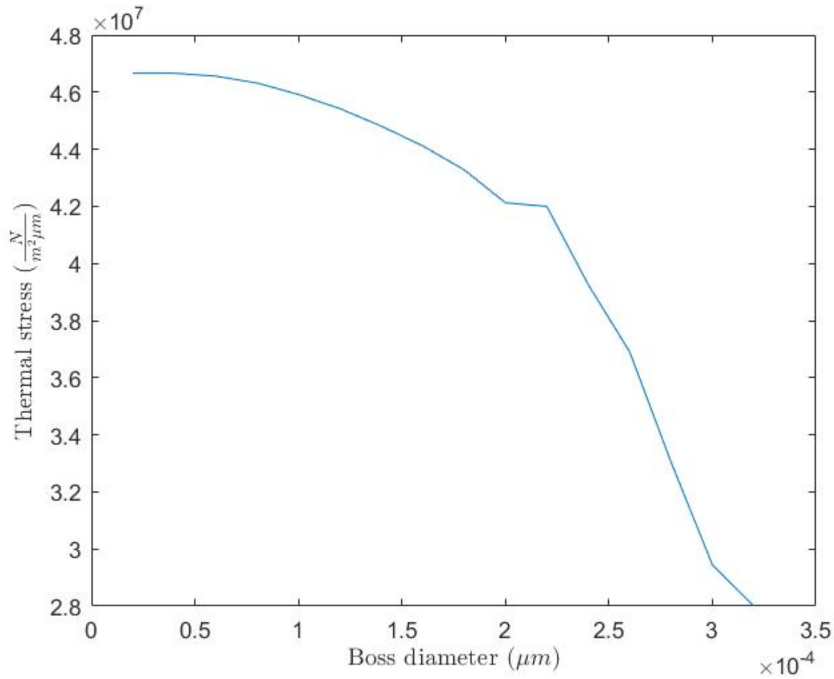

Figure 34: Maximum stress on the membrane due to Thermal expansion for different membrane structures boss diameter

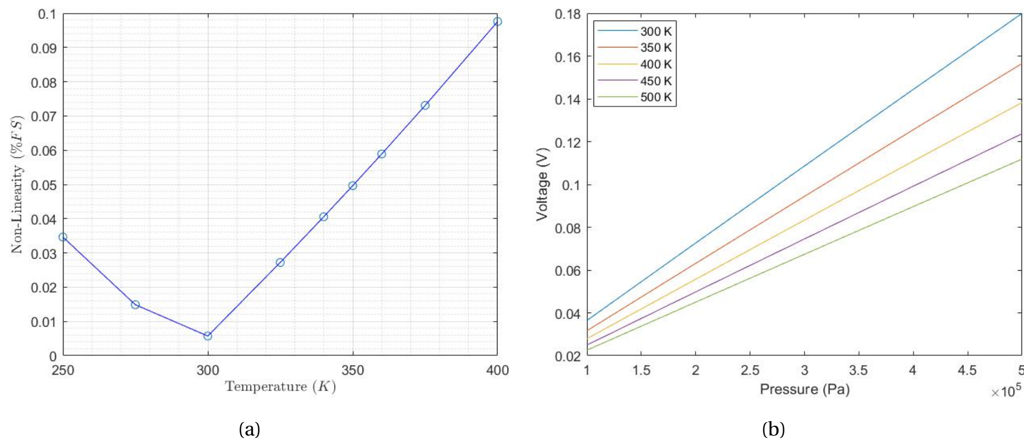

(a)

(b)

Figure 35: a)Non linearity as a function of Temperature for a single boss membrane b)Voltage output at different temperatures

The temperature drift for different boss structures is shown in figure 34. In boss structured diaphragm as temperature changes the TCS effect on the diaphragm is very less due to its rigid silicon boss. So offset drift due to temperature is very less compared to its span values.

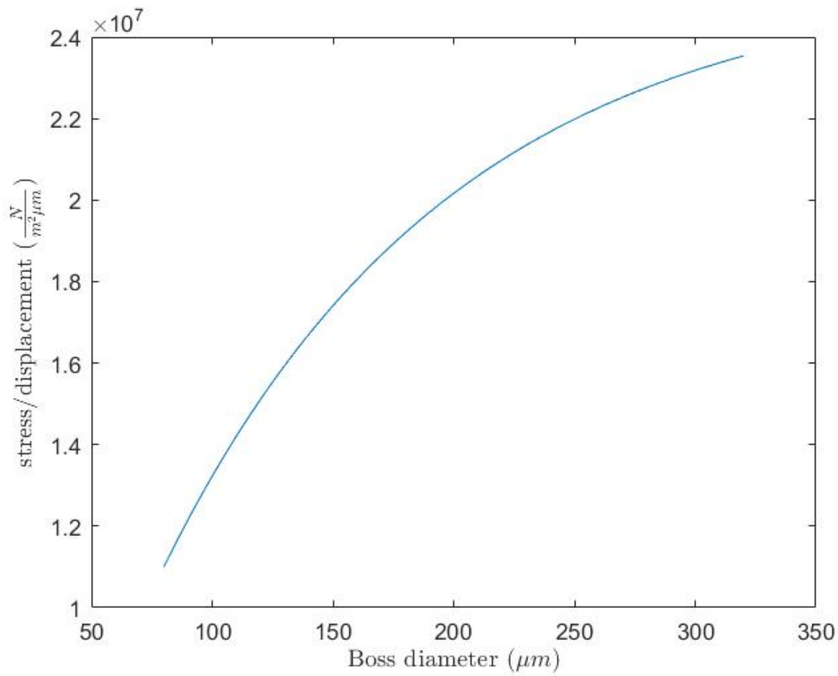

Figure 36: Maximum membrane displacement

4.6.1 Conclusion

A pressure sensor was designed to be integrated in the VLM. The piezoresistive method and a "single boss" membrane structure were employed to achieve the requirements of fast response time and low additional channel volume. The dimensions of the boss structure were optimized to yield maximum linearity. An investigation through FEM simulations showed that the resulting geometry shows 20% lower temperature drift of the output voltage and has 220% higher burst pressure compared to a conventional membrane for the same sensitivity. One potential disadvantage of the bossed geometry is that the interconnect needs to be routed over the membrane which could be a reliability concern. Therefore, the thickness of the aluminum layer needs to be carefully considered or alternatively, a second higher dose implantation must be used to form the interconnect. A to view of the final structure including the interconnect is shown in figure 37 .The temperature sensing resistor is placed on the silicon boss.

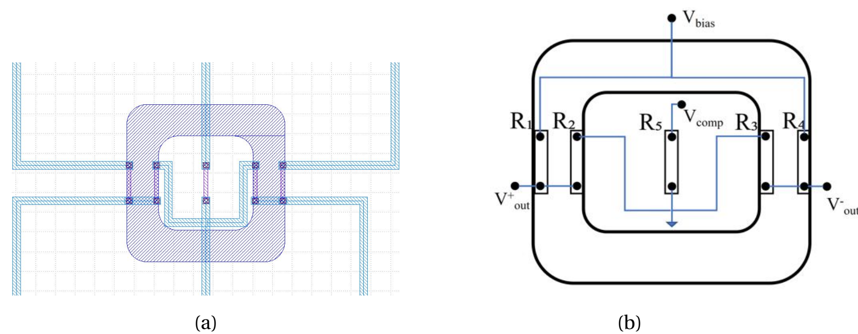

Figure 37: a)2D layout of pressure sensor design including metal interconnect b)Circuit schematic

Although several methods were employed to minimize the temperature dependency of the output voltage (High doping density, bossed membrane, bridge voltage compensation) the proposed design is only expected to have a maximum operating temperature of 150 C^o due to the low bandgap energy of silicon which might be enough to operate the thruster but significantly limits its application range. However the bossed membrane diagram provides regions of opposite

stress and therefore the design can also be implemented polycristaline high bandgap piezoresistors whithout much loss in sensitivity. The designed thrusters can be integrated at multiple points across the channel to evaluate the pressure drop across the heater modules which is an important performance quantity of the vaporization chamber as well as measuring the flow oscillations which are very closely correlated to oscillations in flow and the produced thrust.

5 Processing

Processing is done on 280 μm n-type <100> silicon wafers as well as borosilicate glass for the in-channel structures. Silicon is chosen as the substrate material for the microfluidic channel because of its high thermal conductivity and large range of available processing technologies. High temperature co-fired ceramic technology has also been demonstrated in resistojet applications. Ceramic substrates offer good thermal properties and simpler, lower cost fabrication compared to silicon. However silicon enables the monolithic integration of active devices such as piezoresistive pressure sensors and also the micromachining technologies available for silicon allow the fabrication of complex 3-dimensional structures which is required for this project. The microfluidic channels are capped with glass to enable optical access into the channel which is essential for the calibration of the vapor fraction sensor. Borosilicate glass can bonded to silicon through anodic bonding which is a simple process that doesn't require an adhesion layer and creates strong mechanically robust bonds that can handle pressures up to 20 bar. Finally, processing on glass can be done using standard MEMS technologies for the integration of in-channel structures.

The silicon wafer is processed from the frontside for the integration of the external heaters and pressure sensors while the etching of the microfluidic channels is done from the backside. On the frontside heaters are fabricated on a thin silicon membrane to enhance the heat localization and minimize heat conduction losses. To ensure the structural stability of the structure thicker pieces of silicon must be placed between heaters. The resistors are fabricated inside recesses using multilevel lithography. The borosilicate glass wafer is only processed from the frontside for the integration of the internal heaters and capacitors. Electrical connections to the glass wafer are made by wire-bonding through holes in the silicon wafer. Additional through wafer holes are required in the inlet sections for connection to the propellant tank. Therefore, an etching process needs to be designed that combines through wafer holes with a double depth channel etch for the microfluidic channel and pressure sensor membranes from the backside. For the fabrication of pressure sensors the alignment between the membrane which is etched from the backside and the piezoresistors on the frontside must be very precise. The fabricated thrusters include heater modules separated by pressure and capacitive sensors placed on opposite sides of the channel (see figure 38). A complete list of all process steps can be found in appendix A and the multi image mask layout in appendix B

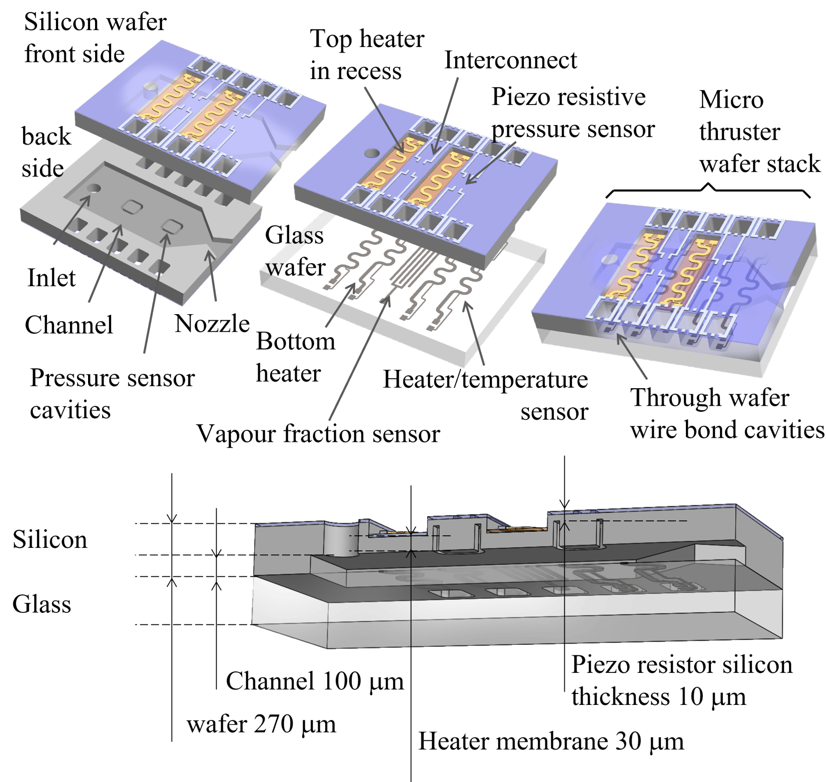

Figure 38: 3D model of fabricated thruster

5.1 Modular fabrication

Devices are fabricated in a modular way meaning that different microthruster designs can be fabricated using the same photomask. This is accommodated by the use of wafer stepper lithography and multi image photomasks. Various heaters and sensors were exposed into the mask so that any combination and number of channels could be connected to reach desired characteristics. This is helpful as for example in a satellite, arrays of thrusters could be integrated each optimized for a different purpose. Devices with longer microfluidic channels can be employed for maneuvers that require high maximum thrust while, shorter channels can be used for maneuvers that require high specific impulse. In this project modular fabrication is used to benchmark different Heater, sensor designs. This is necessary since as was mentioned earlier due to lack of processing power the performance aspects that can be evaluated through simulations are limited. furthermore this modular method enables the combined integration of the modules of this project with other works of TU Delft for future fabrication runs. The diesize is set to match the dimensions of the designed modules: 1 mm X 6 mm. An overview of the designed modules is shown in figure 39 including the metal layers for resistive heaters the metal interconnect, the heater recess, pressure sensor membrane and bonding cavities. Figure 39b shows the layout of the heater module. Bonding cavities are located 100 μm away from the heater recess. Three wire bonding pads are placed on the top silicon surface. Both the silicon and the glass heater need to be connected on the surface of the silicon wafer to expedite the wire-bonding process.

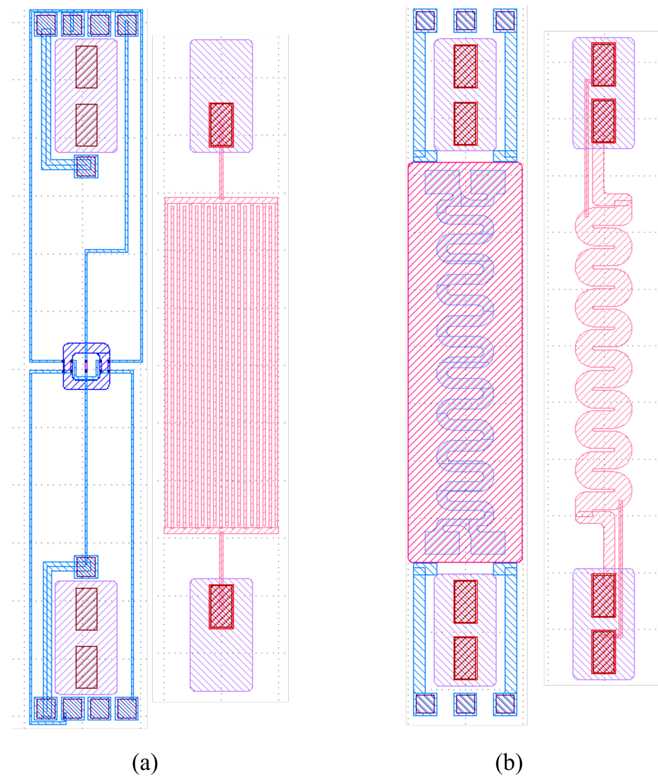

Figure 39: a) pressure sensor-capacitor module mask layout. b) heater module mask layout. left: Silicon frontside , right: glass wafer

5.2 Frontside processing

P-type piezoresistors are formed through ion implantation as it is the most precise method to fabricate shallow doped layers with precise control over the dopant dose. In order to restrict the deposition of impurities to well-defined areas, a thin layer of thermal oxide is grown on the silicon surface to form a barrier to the impurities. The wafer is then masked with photoresist and implanted with boron. A two step implantation (step 1: implantation energy:40 keV dose $4 \cdot 10^{13}$ step 2: implantation energy:80 keV dose $2 \cdot 10^{13}$) is performed to achieve the required dopant concentration of $5 \cdot 10^{18}$ cm^{-3}. A second higher dose implantation is performed at the contact openings to create low resistance ohmic contacts with the aluminum interconnect. Finally, the wafers are annealed at $1100°C$ for 10 minutes to electrically activate the dopants.

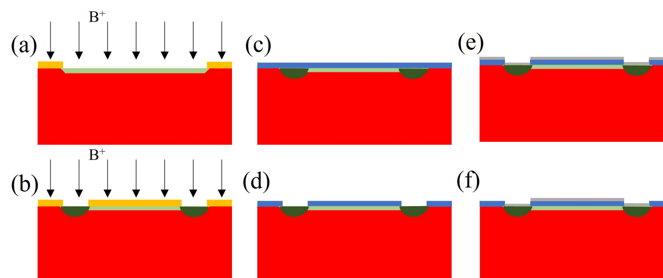

Figure 40: a) mask patterning and boron implantation b)second implantation to from contact pads c)oxide deposition d)etching of contact openings d)aluminum deposition e) etching of aluminum

PECVD TEOS (300nm) is deposited to form an insulation layer. TEOS is removed at the piezoresistor contacts by RIE. An Aluminum layer($2\mu m$) is subsequently deposited through sputtering and patterned to form the interconnect.

Resistive heaters are fabricated on thin silicon membranes. The silicon membrane is fabricated 1st with a silicon etch in the frontside and with the channel etch in the backside. Resistive heaters on thin silicon membranes are a proven concept used for gas sensing applications where μs response times are required however, in this case the membranes are formed by etching silicon from the backside only. Silicon on the front-side of the wafer is etched through DRIE. DRIE through the Bosch process is chosen as the etching method instead of wet etching in KOH because of its vertical sidewall profile which allows a smaller footprint of the module. However, vertical interconnect is difficult to realize and wire-bonding must be used to connect the heater to bondpads on the wafer surface. Because of the large depth of the etch the thickness and choice of masking material needs to be considered. Chemically amplified photo-resist compounds be used to create layers that are sufficiently thick. A $10\mu m$ layer of AZ 12XT photoresist is applied as the masking material. The heater recesses are etched with a depth of approximately $140\mu m$. Next a $2\mu m$ of PECVD TEOS is deposited to act as an insulation layer for the heater. A stack of Titanium (500nm) and aluminum (200nm) are deposited through sputter coating, where the aluminum will be used as an adhesive layer for wirebonding. The aluminum can be etched selectively to titanium by wet etching using a solution of 80% H3PO4, 5% H3NO3,5% HAc and 10% H2O and therefore no intermediate insulating layer is required and corresponding via processing. Since the wafer now has a high topography spin coating of photo-resist is no longer possible. Photoresist is instead applied through spray coating which can be done on an high topography shaped substrate but results in worse homogeneity. With spray-coating the formation of thin and closed resist films becomes more difficult because the landing sites of the droplets follow a statistical distribution. Thus, a minimum critical droplet density is required to allow the aggregation of the droplets to a closed film. Wafers are Spray-coated with 12 (μm) thick AZ12XT photoresist to pattern the metal layers. Because the structures are located below the wafer surface far beyond the depth of focus of the wafer stepper a focus offset is applied during exposure that matches the recess depth. The aluminum wirebonding pads are exposed followed by wet etching. Subsequently, the Titanium resistor is patterned with another step of spaycoating and the Titanium is etched through reactive ion etching. The choice of aluminum for wire bonding pads constraints the maximum operating temperature of the device at 500 C^o which is the melting temperature of aluminum. Final step in the frontside processing is to etch openings on the aluminum interconnect which is covered by the insulating layer of the heaters. TEOS is removed at the pads by dry etching.

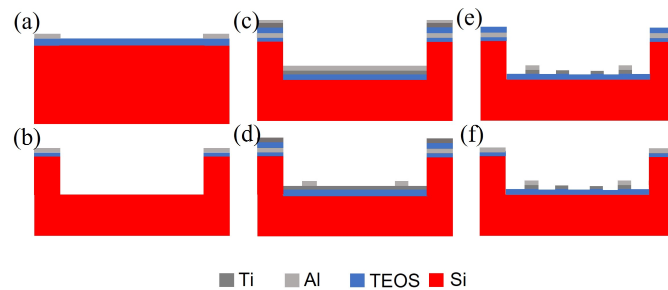

Figure 41: *Microheater fabrication process on silicon a)oxide deposition and patterning of interconnect b)oxide etch, deep silicon etch, c)deposition of TEOS titanium aluminum stack, patterning of aluminum d)etching of titanium e)oxide stripping on interconnect pads*

5.3 Backside processing

The channel patterns inlet holes and pressure membrane etches are performed from the backside. For this etch a conventional single mask process is not sufficient as three different etching depths are required. In the work of [45] a four step etch was performed using a stack of 4 layers ($SiO_2/Al/Photoresist/Al$) that can be etched with high selectivity between them. Similarly in this project a two step etch is performed with PECVD TEOS and photoresist used as masking layers. The photoresist mask is patterned with the structures that require a deeper etch and a through wafer etch, that includes microfluidic inlet, cavities for wire bonding and pressure sensor membranes. The shallower structures for microfluidic channels and nozzles are added on the TEOS hardmask. An etching of approximately $170\mu m$ is performed through the softmask after

which the photoresist is stripped and etching continues through the hardmask for an additional $100\mu m$ .Since the final structure must have two different levels of depth and a through wafer etch, the inlets and bonding cavities are also etched from the front-side. This ensures that by the time the depth of the pressure sensor membrane is reached, the inlets and bonding cavities will be etched completely. A visualization of this process is shown in figure 42. Due to the high heat dissipation during etching, etchers typically provide cooling through flow of helium on the backside of the wafer for temperature control during etching. A landing layer is therefore, required for the through wafer hole etches to prevent the helium from leaking into the reactor chamber. The SiO_2 layer on the frontside can be used as a landing layer because of its high selectivity to silicon. Because of the large dimensions of the openings an additional layer of photoresist is spray-coated to provide structural stability and also to allow the backside hardmask to be stripped in Buffered HF.

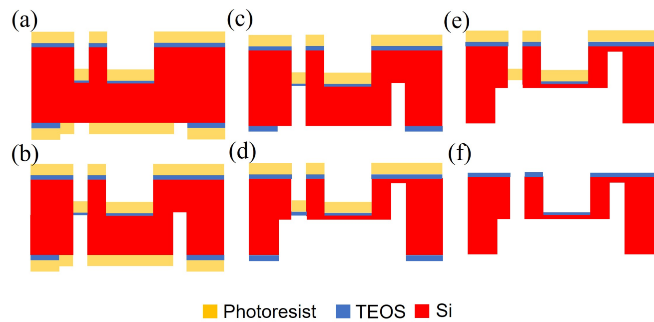

Figure 42: *Backside process a)softmask-hardmask deposition and patterning b)etching of deep structures c)softmask stripping d)etching of shallow structures e)hardmask removal f)landing layer removal*

5.4 Glass processing

Structures fabricated on glass are designed to be as thin as possible as smoother glass surface will require less wafer bonding area. Titanium is used for the resistive layer for the in channel heaters as well as the capacitor electrodes , the bonding pads are coated with aluminum. Titanium is a good candidate for creating structures on glass because of its good adhesion. Titanium (137nm) and aluminum (200nm) are deposited through sputtering .PECVD TEOS is coated as a protective layer to prevent chemical reactions between the metal and the proppelant. Titanium has been shown to oxidize when coated with oxide, therefore 137 nm of titanium is deposited which will result in a conductive layer of approximately 100nm. Finally, the TEOS layer needs to be stripped from the interconect pads and at the areas where the glass wafer comes in contact with the silicon for anodic wafer bonding.

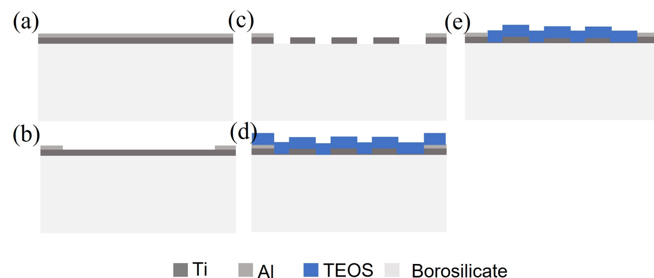

Figure 43: *a)deposition of titanium aluminum stack b) wet etching of aluminum c)dry etching of titanium d)oxide deposition e)etching of oxide outside the fluidic channel area*

5.5 Anodic bonding

The silicon microchannel is enclosed with glass. In previous work silicon to silicon bonding has been demonstrated as well as thermo-compressive bonding of silicon and glass wafers. Thermo-

compressive bonding is a promising solution for achieving high fluidic tightness however it the limits the operating range since thermo-compresive bonds using aluminum peel off at high temperatures. Compared to silicon to silicon bonding, anodic bonding has two main advantages, the heat insulation provided by the glass allows the device to reach higher temperatures while glued on to the PCB and visual access to the channel. Typically, smooth surfaces are required for wafer bonding with surface roughness lower than 10nm. Borosilicate glass becomes flexible at high temperatures and can bend around the metal structures. Borosilicate has a similar thermal expansion coefficient to silicon which means that minimal residual stresses will be induced on the device a bonding. In [4] the strength of the anodic bonds with respect to the width of the bonding area was investigated. A device with a maximum allowable pressure of 7 bar requires $400\mu m$ of silicon around the microfluidic channel. However some delamination is expected around metal structures on glass. For this reason to ensure sufficient bonding strength devices are diced 3mm away from the device edges. This ensures sufficient bonding strength but negatively influences the thermal performance. However the wire-bonding cavities help mitigate this issue as they create additional heat resistance to the surounding silicon outside the channel area. The two wafers are aligned brought into conctact heated up to 400^oC and voltage of 800 V is applied until a charge of 3 mQ is accumulated.

5.6 Critical steps and problems

5.6.1 wafer bonding

Good step coverage of the metal structures on glass is essential to ensure that there is no leakage of propellant through the bonding cavities. Figure 44 shows a microscope image of the bonded wafer taken from the glass side. The brightly colored areas around the metal lines indicate a slight debonding which might lead to leakage at high vapor pressures. The leakage can be sealed by filling the bonding cavities with glue, however its not an optimal solution as it would severely limit the operating range of the device.

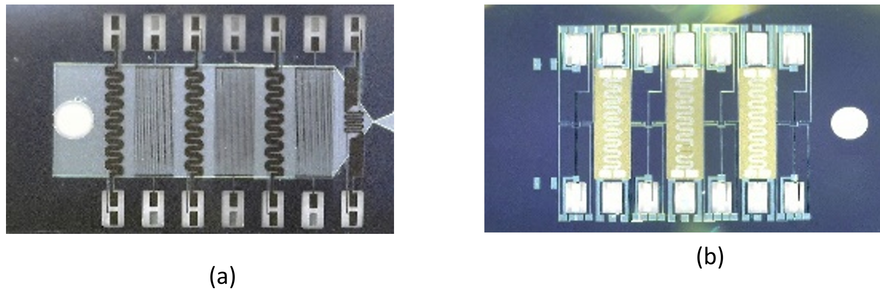

(a) (b)

Figure 44: a)Backside view of fabricated device b)Frontside view of fabricated device

5.6.2 Delamination of photo-resist layer

AZ12XT photoresist is used as a making layer as well as landing layer for DRIE. This generally works but it does not result in a robust fabrication process. Delamination and cracking was often observed which resulted in unwanted etches. On the backside, these cracks can result in additional roughness inside the channel and more fragile devices if they propagate deep enough inside the silicon.

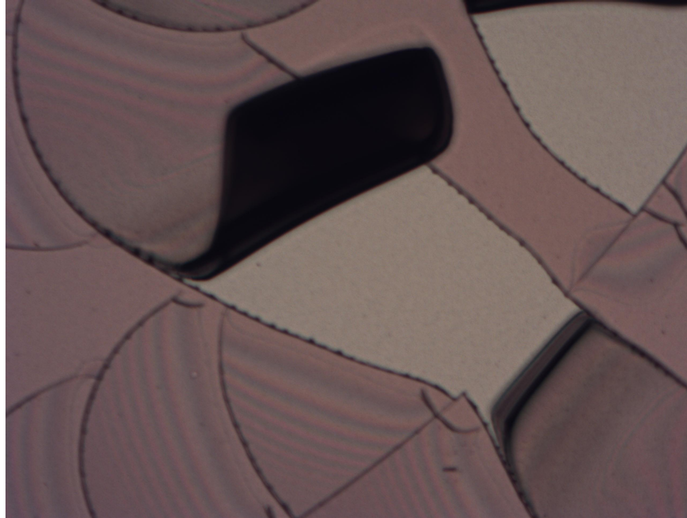

Figure 45: Cracks and delamination on soft-mask after DRIE

5.6.3 Broken oxide membranes on inlet holes and bonding cavities

Breaking and cracking of the landing layer was observed after removing the backside soft-mask. Removing photo-resist from only one side of the wafer proved to be unreliable as the thin oxide membranes would often crack. Possible solution to this problem is applying a thicker SiO_2 layer or to use a less brittle insulating material below the heaters. The issue with this is that the depositions in surfaces with deep cavities might result in poor step coverage meaning that it would be impossible to create a mechanically robust membrane as the deposition rate close the edges is very low. For a more reliable process laminated photoresist can be applied after the first step of the backside etch to act as the landing layer

5.6.4 Mask undercut

In the second step of the backside etch pressure sensor membranes and channels are etched simultaneously. The pressure sensor etch has to continue without a mask as it is located inside the channel . In theory this should not be a problem as the sidewalls are masked by the passivation layer during the DRIE process. However a significant increase in the width of the opening was observed during the second etch (see figure 46). Which means that the two mask stack method might not be a viable way of fabricating these devices. Instead the two masks might need to be applied separately(one before each etching step) using spray coating.

5.6.5 DRIE

Etch rate of the DRIE process becomes dependent on the width of the mask opening for opening narrower than approximately $200\mu m$. In addition, the etch rate slows down with larger depth. The pressure sensor etch is deeper and also has smaller mask openings which means that pressure sensors are etched slower compared to the vaporization chamber. For this reasons the process would be more reliable with the inclusion of SOI wafers. Having a stopping layer for the pressure sensor etch would allow precise determination of the membrane thickness while still having control of the channel depth.

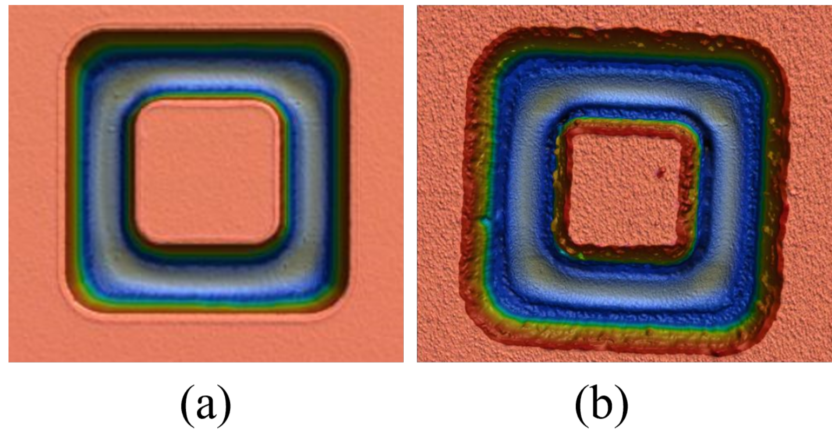

Figure 46: a) pressure sensor membrane after first etch b) pressure sensor membrane after second etch

5.7 Assembly

5.7.1 PCB attachment

To perform measurements the VLM is attached on a PCB which is specifically designed for this application. A 4mm wide gap is placed underneath the VLM through which the fluid flow can be monitored through the glass wafer. Fluid motion, as well as phase change phenomena, could provide very useful information about the performance of the heating chamber. Design of the PCB was kept as straightforward and compact as possible. The layout of the PCB is shown in figure 47. Connections are made through both the top and bottom surface to accommodate the high wiring density. All bondpads are located at the frontside.

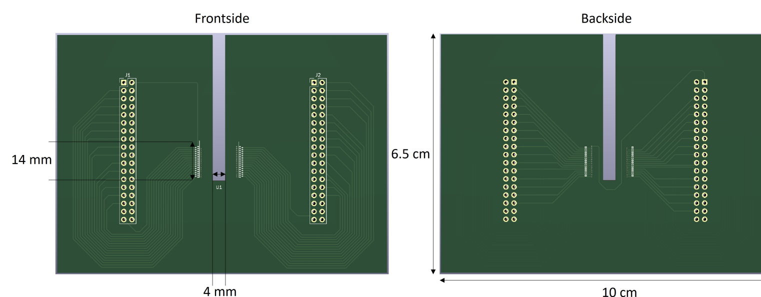

Figure 47: PCB Layout

The die is attached on the the PCB using glue which is then cured at 150C ^{o}C for 2 hours. The PCB is made of standard FR4 material which can withstand temperatures up to 120 ^{o}C. However because of the high heat resistance of the glass wafer the channel walls can be heated up to higher temperatures. Electrical connections to the PCB are made through wedge bonding of aluminum wires with diameter of 25 μm. The current VLM design requires a relatively high wirebonding density (3-4 bonds per 1 mm) and wires with lengths over 3mm. For testing, not all heaters and sensors will be wirebonded as this would result in very fragile devices instead different sensor-heater combinations are wirebonded on different devices. Epoxy resins could be used to provide mechanical stability for the wires and prevent contact between them but it also limits the maximum temperature of the heaters to 120 ^{o}C.

5.7.2 Connection to microfluidic interface

The fabricated VLMs' inlet must be connected to the fluid supply without any leakage or obstruction to the free flow of the propellant. A metal microfluidic tip is attached using adhesive which is then cured at 120°C for two hours to create the microfluidic interface . No leakage was observed

when applying liquid flow at inlet various inlet pressure levels. Unfortunately, the final structure is very fragile and must be handled with caution.

For testing purposes the requirement for high temperature materials does not apply for the microfluidic interface. However, due to the large heat resistance between micro-heaters and the silicon substrate that provided by the proposed design a large temperature difference is expected between the vaporization chamber and the inlet sections which allows flexibility in choosing materials to form the microfluidic interface.

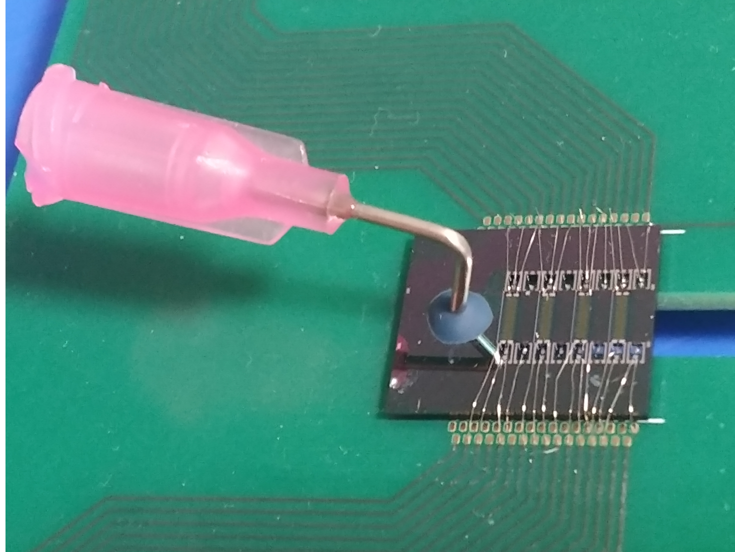

Figure 48: VLM with fluidic inlet attached adhesively

5.8 Summary

In this chapter the fabrication process for the VLM was presented. A fabrication process was proposed for fabricating multi-detph silicon structure that includes combines front-side etching and a two step backside etch. Furthermore structures were fabricated inside recesses by spray coating photo-resist and applying a focus offset to the exposure. Micricrofluidic channels with internal structures were fabricated by employing a simplified process that includes anodic bonding and no adhesion layer. The resulting devices showed sufficient fluidic tightness. The process showed a very high yield and most of the devices had a clear and sharp structure with the specified dimensions, however, there were several minor problems which were previously discussed. This process could be used in the future and further developed for integration of MEMS VLM modules. Finally, the process can be improved with the use of different recipes for DRIE the inclusion of SOI wafers and employing more robust photoresist compounds for masking during deep etching.

6 Characterization

In this chapter testing and verification of the heating performance in the vaporization chamber and calibration of the sensors is presented. Regarding the heater perfromance the first step is to verify that the TCR matches the expected values. This will verify that the resistors are functional and that nothing unexpected happened during fabrication. Heating performance is evaluated by applying power to the resistors and measuring the temperature at different flow rates. Furthermore, the stability of the two phase flow is evaluated through visual observations through the glass. Optical images captured by a camera are also used to calibrate the vapor sensors. The pressure sensor is calibrated by applying a known pressure and measuring the voltage output. As a final step sensor data is recorded during operation of the thruster. A schematic of the experimental setup is shown in figure 49

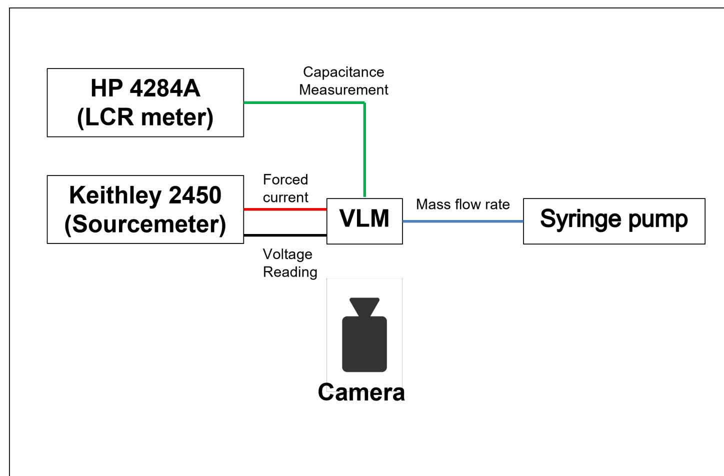

Figure 49: Experimental setup used for characterization

6.1 Sensor calibration

6.1.1 RTD/heater characterization

A wafer with completed heaters is loaded on a temperature controlled chuck of a probe station Each heater/resistive temperature detector (RTD) is characterized by applying constant current and measuring its resistance through a four probe measurement. A series of measurements is performed. For each measurement the probestation chuck is heated up to a given temperature on a gold chuck which is uniformly heated up to 200 ^oC. The measurement data is linearly interpolated using

$$R = R_0(1 + a(T - T_0)) \tag{58}$$

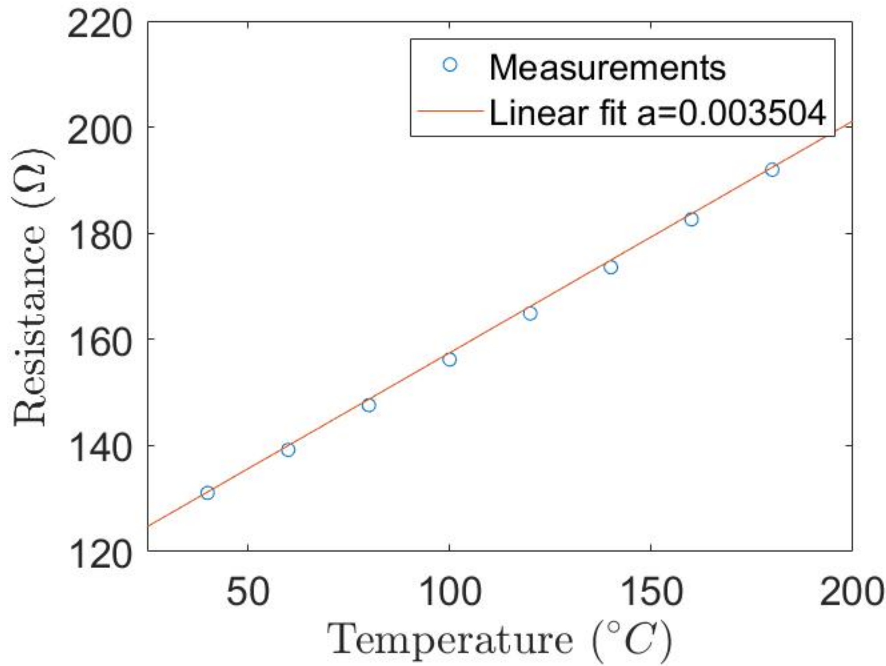

Figure 50: RTD calibration

The resulting interpolation curve is shown in figure 50. The TCR was measured to be 0.0035 $1/^{o}C$ with a high degree of confidence (R = 0.997). This confirms that over the temperature range a linear approximation is valid. It should be noted that calibration was performed with a uniform temperature over the heater area, in real operational conditions this will be different.

6.1.2 Vapor fraction section calibration

For the calibration of the capacitive vapor sensor, optical images are used to estimate the amount of vapor in the channel. The images are taken through the glass from the backside through the integrated capacitive sensor in the channel. Calibration of the vapor sensor is performed by correlating the amount of vapor to the measured capacitance. The camera is slightly tilted with respect to the glass surface to create better visual access behind the interdigitated capacitor electrodes. Images are captured with a frequency of 20Hz and cropped to only include the sensor area and converted to gray-scale. At each pixel point, the image grey level was discretized on 256 grey levels (using 8 bits), defining the full dark condition (low luminosity) and the full bright condition (high luminosity). The image data-set was processed using Matlab the gray-scale raw image is enhanced to increase the contrast, smoothed by convolving with a Gausian kernel and converted to a relative luminance, ranging between 0 and 1. The image corresponding to full liquid flow is used a reference for computation of the relative luminance as an attempt to compensate for non uniform illumination .By computing the average luminance of the image an estimation of the vapor fraction is obtained. The correlation between the luminance signal and the capacitance is used to calibrate the sensor. Figure shows the average luminance signal and measured capacitance signal. The capacitance drops from 55 pF to 5 pF as the flow turns from liquid to vapor. Significant amount of noise is present on the capacitive measurement with an average value of 4 pF this however much lower compared to the dynamic range of 40 pF. The two signals are highly correlated

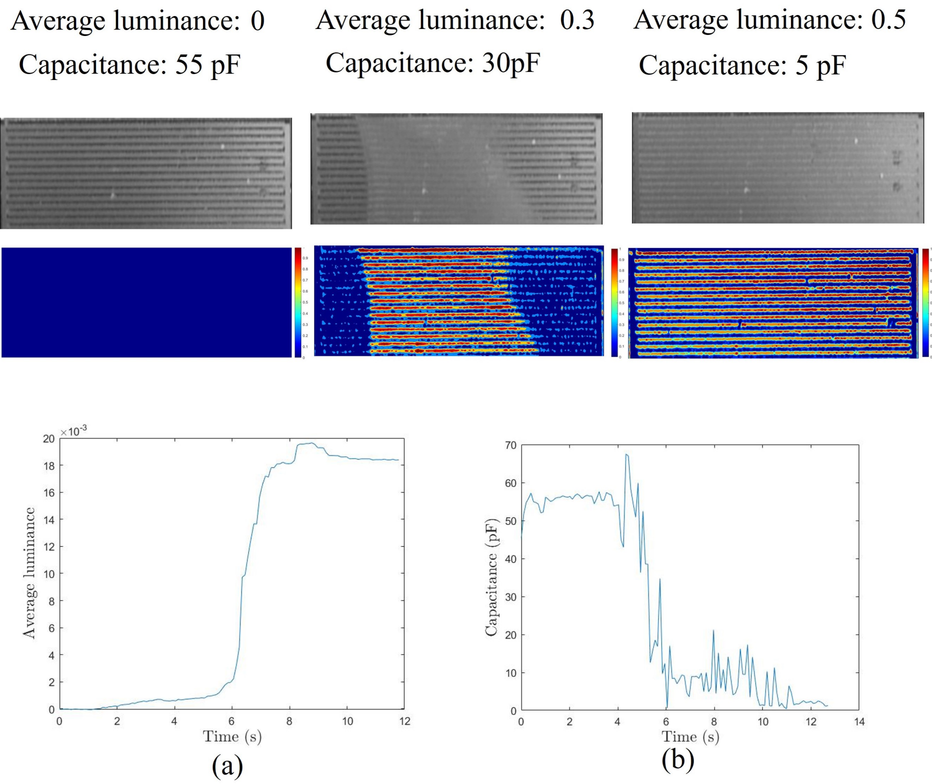

Figure 51: a)Average luminance over vapor sensor area during phase transition b)Measured capacitance during phase transition

6.1.3 Pressure sensor Calibration

Calibration of the pressure sensor is performed on a test device that does not include an outlet. A known pressure is applied at the inlet which in the absence of flow can be considered to be uniform inside the chamber. The Wheatstone bridge is biased at 5 V and output voltage is shown in figure 52. The measured sensitivity is approximately 2 mV/bar and the noise amplitude in the measured signal is 16 μV which corresponds to a resolution of 0.08 bar. The non-linearity and lower sensitivity which is observed when the pressure is increased above 5 bar can be partially attributed to fluid leakage at the inlet and also bending of the membrane. When applying a constant pressure of 6 bar the output voltage begins to drift to higher values indicating possible plastic deformation of the membrane. When applying pressure higher than 7 bar the channel bursts open on the silicon side. The measured sensitivity is much lower compared to the simulated result. This large deviation is mainly caused by non-ideal etching which resulted in a curved membrane thickness profile. The membrane has a minimum thickness of 10 μm at the center which increases to 20 μm at the edges resulting in lower induced stress magnitude and wider maximum stress regions. A comparison of the stress profile on the fabricated membrane and the designed one is shown in figure 53. The results showed that integration of the pressure sensor is possible however the fabrication process needs to be improved with better DRIE recipes or by processing on SOI wafers.

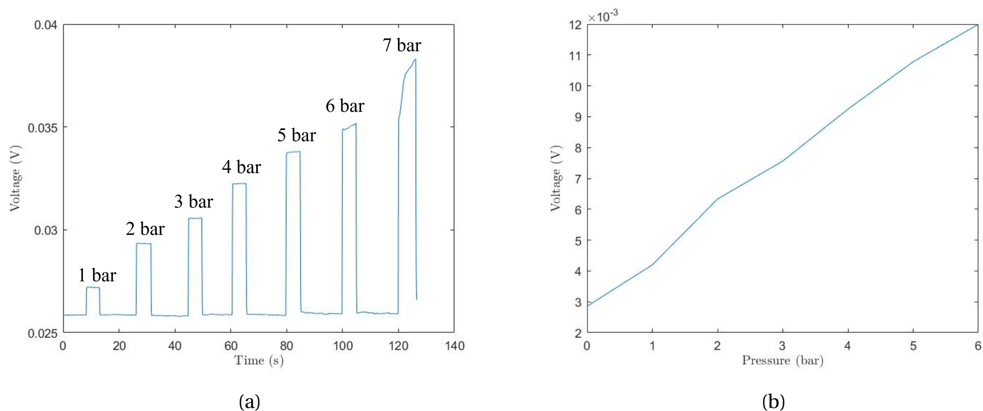

(a)

(b)

Figure 52: Pressure sensor voltage out. The Wheatstone bridge is biased at 5V

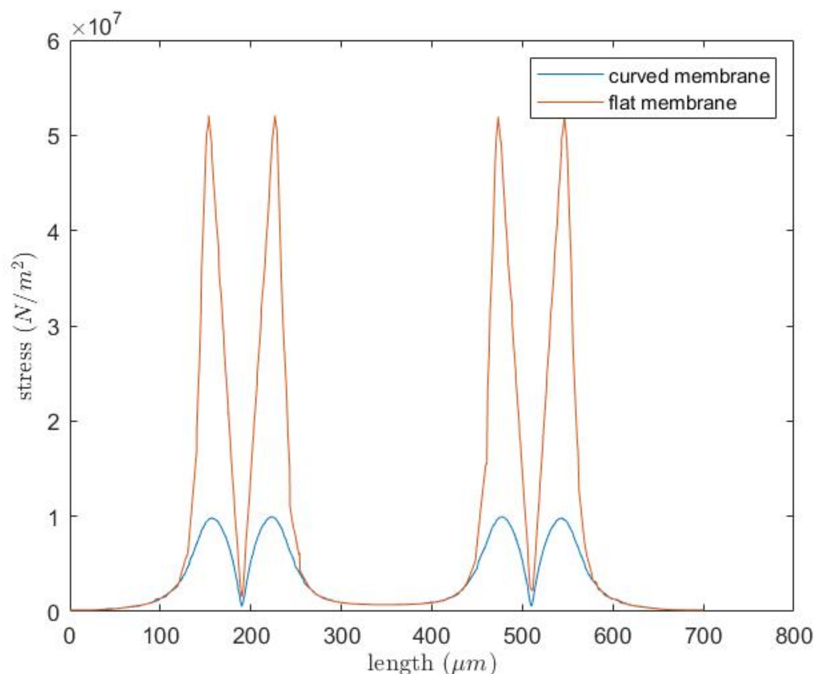

Figure 53: Comparison of the simulated stress profiles between the designed membrane and the fabricated membrane

6.2 Heater performance

It is observed that the relation between temperature and applied voltage is non-linear which is in accordance with the non-linear increase in resistance. Consequently, the lower the supplied voltage is, the lower the load resistance is and the faster the device temperature response is. With the increase of temperature, the resistance of the heater increases and, as consequence of this, a smaller temperature variation is obtained as the heater power increases. Figure 54 shows the I-V curves of the heater for dry conditions and a flow of (1mg/s) delays are included in-between measurements at different current levels to allow the system to reach thermal equilibrium. In addition, it should be considered that the heat transfer between the device and the ambient or the PCB introduces secondary non-linearities in temperature-heater resistance relationship. The heat resistance of the micro-fluidic channel can be derived from the difference in temperature between dry and wet conditions for a given input power.

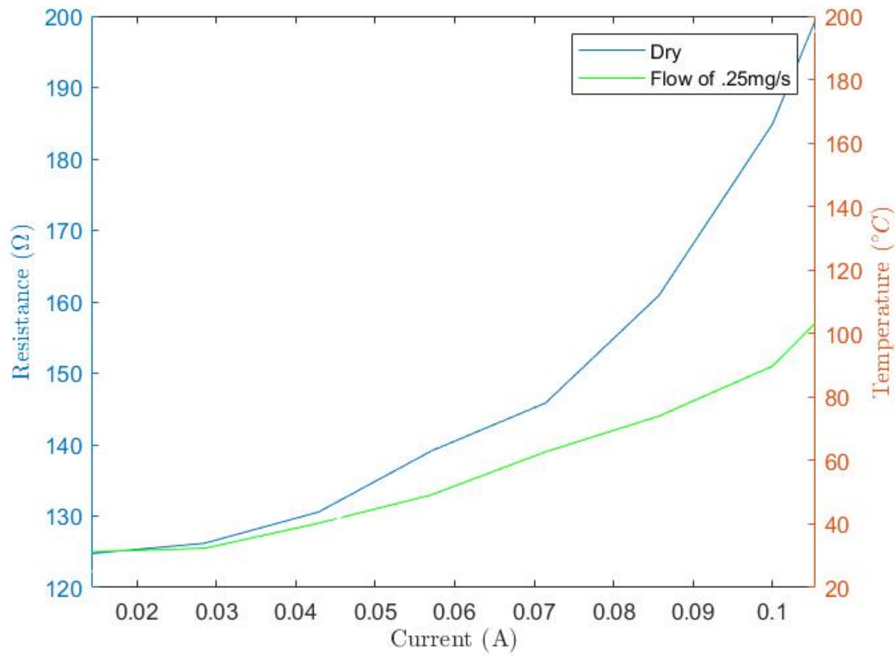

Figure 54: Measured temperature at different power levels for a single heater module

Figure 55 shows the temperature response of the heater module at different power levels for dry condition and flow of $1 mg/s$. In the presence of liquid the the time response is sharper as is expected from equation 30.

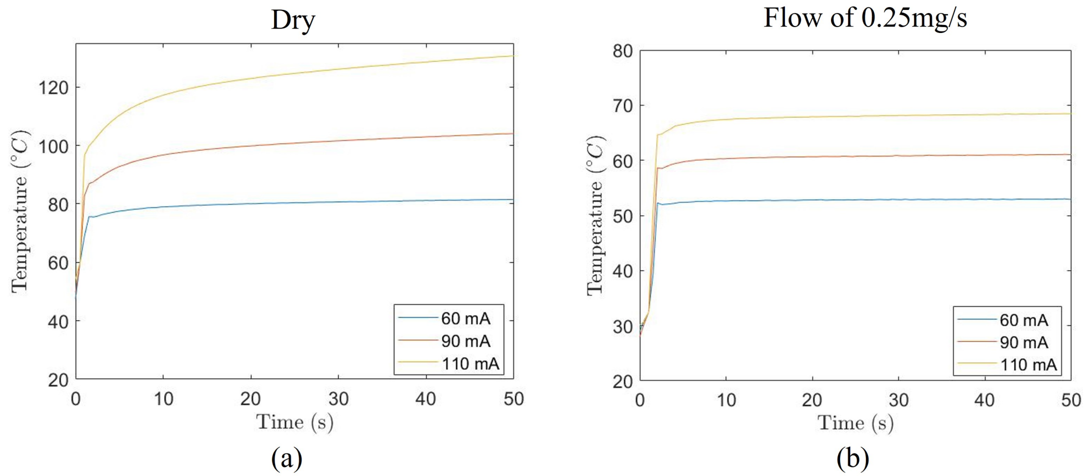

Figure 55: Time response of heater temperature in wet and dry conditions

The input power P_{in} required to fully vaporize the flow and provide a sufficient amount of vapor given a certain flow rate is determined using measurements of the capactive sensor. A given and fixed flow rate is applied and the power on the heaters is increased until the capacitance drops to its minimum value. A device with four heater modules separated by capacitive sensors is used. The capacitance is measured at the sensor that is located closest to the nozzle exit (see figure 56). Results are shown in table 5. The power needed for vaporization is relatively high. However it should be noted that the pressure at the inlet required to force the flow is very low (0.8 bar at 1 mg/s) therefore a longer thruster with a larger number of heater modules could be fabricated using the modular fabrication method to achieve better results. The vapor temperature at the nozzle is approximately 180 ^oC

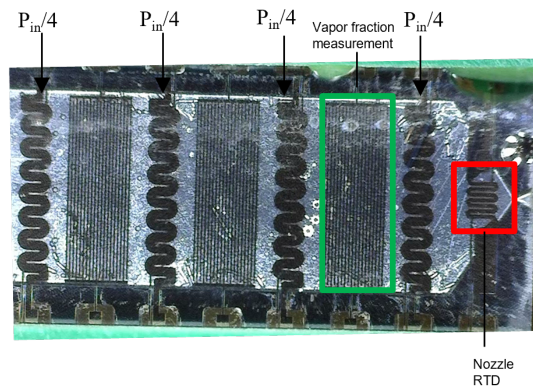

Figure 56: Thruster used for heater performance evaluation, seen from backside

Table 5: *Power required to operate the thruster flow for a given mass flow rate*

Flow rate	0.2 mg/s	0.4 mg/s	0.6 mg/s	0.8 mg/s	1 mg/s
Power	1.9 W	3 W	5 W	6 W	8.2 W

The heater temperature and corresponding vapor fraction measured by the sensor that is directly in front of it is shown in figure 57. Approximately, at time 0 the heater is turned on. A large difference in heat rate is observed a the flow turns from liquid to vapor. While the flow is fully vaporized the heater temperature remains constant at approximately 200 ^oC. At 40 s power reduced and two phase flow starts appearing. Significant oscillations in vapor quality and heater temperature are observed until the flow settles to full liquid at which point the heater temperature drops sharply. The vapor sensor gives valuable information about the performance. Figure 57 shows the clear relation between the vapor fraction and heat transfer coefficient and can therefore be used to optimize the power input to the heater in order to deliver the most power possible without overheating.

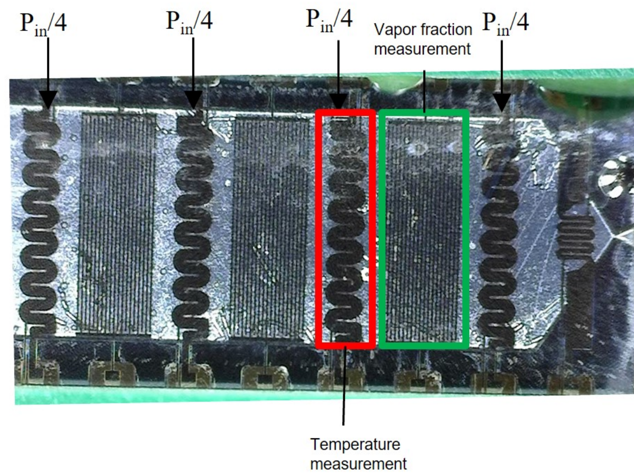

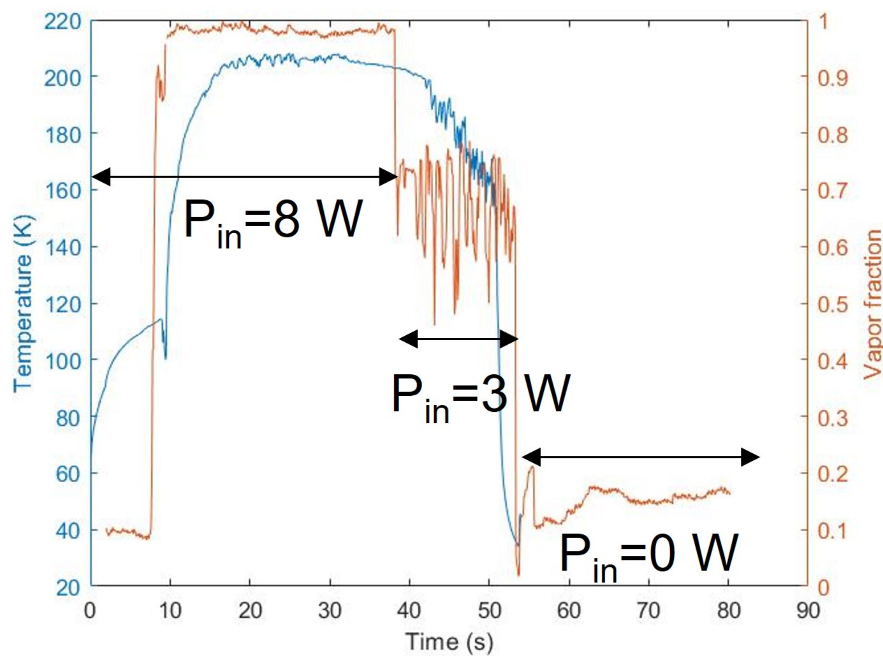

Figure 57: Measured temperature and vapor fraction

6.3 Flow observations

Figure 58a) shows the flow as seen from the backside for low input power and low flow rate. The thruster includes four heater modules and the input power is evenly distributed between them. Bubbles grow rapidly inside the area of the heaters. After reaching the channel height the bubbles begin to elongate until they exceed the heater area at which point they detach and flow downstream. When increasing the input power the bubbly flow becomes more unstable with bubbles appearing stationary and the flow moving in all directions. Figure 58b) shows the flow when only the third heater is operating. Bubbles are only observed downstream from the heater demonstrating that there is significant heat resistance between heaters.

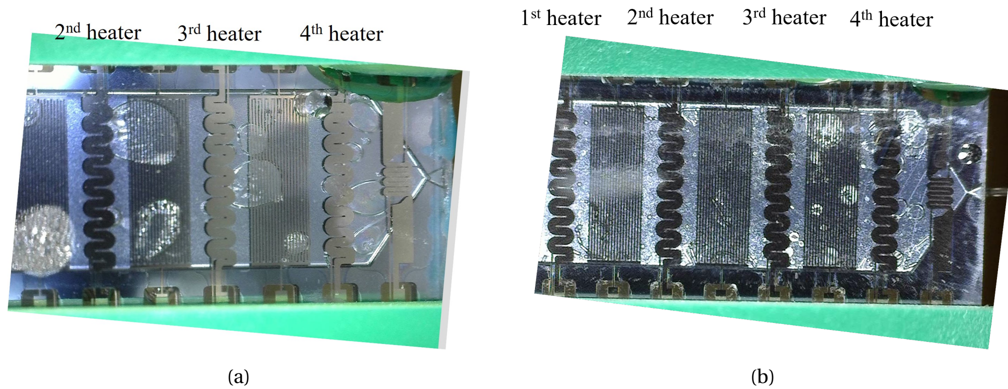

Figure 58: a)bubbly flow with all 4 heaters operating b)Bubbly flow hen only the third heater is operating

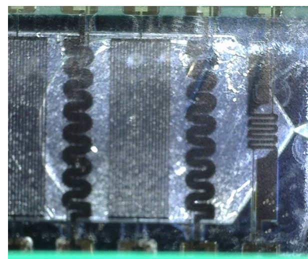

Figure 59: Possible stable condition

When increasing the applied power so that the flow is fully vaporized bubbling phenomena are no longer observed instead there is a clear vapor-liquid interface. The amount of vapor in the channel oscillates and the vapor-liquid interface constantly moves back and forth. It should be noted that the heaters are operated by applying either constant voltage or constant current. Because of titanium's positive TCR applying constant voltage causes the power to drop as the temperature increases this leads to a condition where the flow constantly switches between liquid and vapor. Whereas constant current can lead to thermal runaway since power increases with temperature. To mitigate instabilities the thruster can be integrated with a constant power converter like those reported in [46] or with the implementation of temperature feedback. Possibly stable flow was observed when varying the distribution of power between heaters. In this case the largest percentage of power is delivered in the third heater with the first two heaters only used for preheating the liquid. This creates a sharper transition between vapor and liquid and more stable flow (see figure 59). The fourth heater can be used to further super-heat the vapor. This result is in agreement with the observations of [20] which showed that stable flow is observed in a certain range of inlet subcooling, heat flux and mass flux conditions.

6.4 Conclusion

In this chapter the calibration of sensors and a partial characterization of the heat transfer performance and flow in the microfluidic channel was presented. Vapor and temperature measurements were recorded during operation of the thruster. The proposed vaporization chamber design posseses the ability to vaporize the flow and superheat the vapor . The vaporization chamber was designed with low pressure loss and uniform heat flux as requirements. For certain conditions of applied heat flux and flow rate the vaporization behaviour was observed to be relatively stable. No bubble related failure modes were observed and the oscillations in wall temperature were minimal. Silicon was removed to reduce the thermal mass of the heaters and allow fast temperature response while maintaining the mechanical strength to withstand pressure up to 5bar. Because of the very low pressure drop in the channel (flow of 1mg/s can be vaporized at an inlet pressure of 1-1.1 bar) a lot more silicon can be removed to make the response even faster and more suitable for temperature control, pulsed heating modes of operation. The integration

of pressure sensors was proven to be successful however because of the issues during etching which were discussed in the fabrication section the performance is not sufficient for practical application and the pressure drop along the vaporization chamber could not be measured. The capacitive sensors were proven to be very sensitive devices that can be used to accurately determine the vapor fraction. Vapor fraction measurements were recorded during operational conditions and it was shown that vapor sensing can provide important insight into the operation of the VLM and could be used to implement feedback control of the input power to optimize heating efficiency. The proposed manufacturing process showed successful integration of micro-heaters with pressure sensors and vapor fractions sensors and as such can be a manufacturing platform for VLMs.

7 Summary

The design and wafer-level fabrication of a water propellant vaporizing liquid microthruster (VLM) was presented. The main goal of this work was to address intrinsic instability of VLMs caused by the stochastic nature of boiling and the viscous effects in the microscale. Monolithically integrated sensing was added to the VLM which provides insight in the boiling process and allows the implementation of feedback control. The thruster was fabricated with a conventional anodic bonded silicon-glass wafer stack with a glass capped microfluidic channel, in-channel heaters and sensors on the glass wafer were combined with on-channel heater and sensors on the silicon wafer. The vaporization chamber was designed with fast response time, low pressure drop and stepwise heating in mind. The pressure drop in the channel is dictated by the hydraulic diameter of the structure. Therefore it was decided to keep it large and not include any internal fin structures. To create sufficient thermal contact resistive microheaters were integrated on both sides of the channel. Furthermore, the shape of the resistors was optimized to compensate for the heat loss at the channel edges and create a more uniform temperature distribution. Silicon was removed at the location of the heaters from the front-side of the wafer bringing the heater closer to the channel and improving the time response. This also has the advantage of control over the channel height without affecting the conduction loss. This particularly useful for the design of the planar vapor sensor since the channel height can be adjusted to be compatible with the vapor sensor's probing depth. Vapor sensors were designed as planar interdigital capacitors placed on glass and integrated in parallel with a pressure sensor on the silicon side. The proposed pressure sensor design includes piezo resistors which are suitable for measuring the sharp pressure changes that result from explosive boiling phenomena and a "bossed" membrane structure that minimizes the added channel volume and effect of thermal stress. A preliminary characterization of the the heaters and integrated sensors was presented which provides sufficient proof that the integration was successful. More work is needed though to derive a full characterization.

7.1 Future work

Temperature control
The resistive micro-heaters were designed to include 4 interconnect pads to accommodate 4 probe resistance measurements. As discussed in the characterization section the input power to the heaters varies because the resistance changes with temperature which deteriorates the stability of the thruster. Therefore the implementation of a temperature feedback controller is crucial for maintaining steady heat flux delivery in the microfluidic channel and could lead to significant performance improvement.

Optimization of heating strategy
One of the main achievements in this project was the fabrication of heaters with significant heat resistance between them that enables step-wise heating .The optimal method of heating up the flow however still needs to be investigated. This can be done by introducing feedback control using the integrated sensors. Furthermore it would be worth investigating pulsated modes of operation. Pulsed operation of the heat flux has shown potential to increase heat transfer dramatically. Finally, an appropriate control interface needs to designed that includes a microcontroller and a measurement board that is capable of simultaneously performing multiple capacitive and resistive measurements.

Packaging
The final product fabricated needs to be packaged for mechanical stability and energy efficiency. There are a variety of options to achieve that. Air gap packaging is a promising option to achieve high heat insulation. A layer of air is used as an insulating layer between the silicon surface and package. The package can be attached using high temperature glue allowing the device to operate at temperatures up to the melting point of the metals. However it doesn't provide any mechanical stability for the wirebonds. An alternative solution that could be investigated is glass-silicon-glass configuration. Two glass wafers could be anodically bonded to the silicon wafer as was demonstrated in [47]. The resulting structure could be packaged further by standard processes like applying mold. This will further improve thruster performance by creating a very high thermal barrier for the power generated by the microheaters while also providing protection for

the wirebonds.

Fluidic interface

The fluidic interface needs to be improved in terms of mechanical robustness and flow establishment. The fluidic inlet used in this project is only intended for testing purposes since it is too fragile for practical applications. Furthermore this method of introducing a flow through a vertical hole in the silicon wafer in combination with the imprecise attachment process of the inlet can lead to poorly established flow leading to deterioration of the thermal performance. Methods of horizantally attaching the inlet need to be investigated with an inlet chamber structure that that creates uniform distribution of the flow

References

[1] A. Camps, 'Nanosatellites and Applications to Commercial and Scientific Missions', Satellites Missions and Technologies for Geosciences. IntechOpen, Jul. 22, 2020. doi: 10.5772/intechopen.90039.

[2] Kristina Lemmer,Propulsion for CubeSats,Acta Astronautica, Volume 134,2017,Pages 231-243,ISSN 0094-5765,https://doi.org/10.1016/j.actaastro.2017.01.048.

[3] Liu B, Li X, Yang J, Gao G. Recent Advances in MEMS-Based Microthrusters. Micromachines (Basel). 2019 Nov 26;10(12):818. doi: 10.3390/mi10120818. PMID: 31779202; PMCID: PMC6953018.

[4] Müller, Jürgen Tang, William Wallace, Andrew Lawton, Russel Li, Wen Bame, David Chakraborty, Indrani. (1997). Design, analysis and fabrication of a vaporizing liquid microthruster. 10.2514/6.1997-3054.

[5] Mukerjee, E.V.; Wallace, A.P.; Yan, K.Y.; Howard, D.W.; Smith, R.L.; Collins, S.D. Vaporizing liquid microthruster. Sens. Actuators A Phys. 2000, 83, 231–236

[6] Ye, X.Y.; Tang, F.; Ding, H.Q.; Zhou, Z.Y. Study of a vaporizing water micro-thruster. Sens. Actuators A Phys. 2001, 89, 159–165.

[7] Kwan, P.K.; Huang, X.; Zhang, X. Design and testing of a microelectromechanical-system-based high heat flux vaporizing liquid microthruster. Acta Astronaut. 2020, 170, 719–734

[8] Liu, B.; Li,W.; Yang, X.; Yang, J.;Wang, Y.; Li, D.; Gao, G. A new vaporizing liquid microthruster with planar induction heating. Sens. Actuators A Phys. 2020, 308, 112010

[9] Fontanarosa, D.; de Pascali, C.; de Giorgi, M.G.; Siciliano, P.; Ficarella, A.; Francioso, L. Fabrication and embedded sensors characterization of a micromachined water-propellant vaporizing liquid microthruster. Appl. Therm. Eng. 2021, 188, 116625.

[10] Kundu, P.; Bhattacharyya, T.K.; Das, S. Design, fabrication and performance evaluation of a vaporizing liquid microthruster. J. Micromech. Microeng. 2012, 22, 1–15.

[11] Cen, J.W.; Xu, J.L. Performance evaluation and flow visualization of a mems based vaporizing liquid micro-thruster. Acta Astronaut. 2010, 67, 468–482.

[12] C.-C. Chen, H.-C. Kan, M.-H. Lee, C.-W. Liu Computational study on vaporizing liquid micro-thruster 7th International Microsystems, Packaging, Assembly, and Circuits Technology Conference, (IMPACT) (2012), pp. 68-71

[13] M. Mihailović, C. Rops, J.F. Creemer, P.M. Sarro MEMS silicon-based micro-evaporator with diamond-shaped fins, Procedia Engineering Eurosensor XXIV Conference (2010)

[14] M.A.C. Silva, D.C. Guerrieria, H. van Zeijlb, A. Cervone, E. Gill Vaporizing liquid microthrusters with integrated heaters and temperature measurement

[15] G. Wang, P. Cheng, H. Wu, Unstable and stable flow boiling in parallel microchannels and in a single microchannel, Int. J. Heat Mass Transf. 50 (2007) 4297–4310.

[16] Qi Jin, John T. Wen, Shankar Narayanan, Temperature synchronization across parallel microchannels during flow boiling, International Journal of Thermal Sciences, Volume 156, 2020, 106476, ISSN 1290-0729, https://doi.org/10.1016/j.ijthermalsci.2020.106476.

[17] Aguiar, Gustavo. (2017). An experimental study on flow boiling in single microchannels subjected to localized cyclical heating loads. 10.13140/RG.2.2.24589.79840.

[18] Todd A. Kingston, Justin A. Weibel, Suresh V. Garimella, Time-resolved characterization of microchannel flow boiling during transient heating: Part 2 – Dynamic response to time-periodic heat flux pulses, International Journal of Heat and Mass Transfer,Volume 154,2020,119686, ISSN 0017-9310,

[19] Kingston, T.A.; Weibel, J.A.; Garimella, S.V. Time-resolved characterization of microchannel flow boiling during transient heating: Part 1—Dynamic response to a single heat flux pulse. Int. J. Heat Mass Transf. 2020, 154, 119643

[20] G. Wang, P. Cheng, H. Wu, Unstable and stable flow boiling in parallel microchannels and in a single microchannel, Int. J. Heat Mass Transf. 50 (2007) 4297–4310.

[21] Jinliang Xu, Guohua Liu, Wei Zhang, Qian Li, Bin Wang, Seed bubbles stabilize flow and heat transfer in parallel microchannels, International Journal of Multiphase Flow, Volume 35, Issue 8, 2009, Pages 773-790, ISSN 0301-9322, https://doi.org/10.1016/j.ijmultiphaseflow.2009.03.008.

[22] Aguiar, Gustavo. (2017). An experimental study on flow boiling in single microchannels subjected to localized cyclical heating loads. 10.13140/RG.2.2.24589.79840.

[23] Baroncini M, Placidi P, Cardinali GC, Scorzoni A (2004) Thermal characterization of a microheater for micromachined gas sensors. Sens Actuators A 115(1):8–14

[24] Mele L, Rossi T, Riccio M, Iervolino E, Santagata F, Irace A, Breglio G, Creemer JF, Sarro PM (2011) Electro-thermal analysis of MEMS microhotplates for the optimization of temperature uniformity. Proc Eng 25(35):387–390

[25] Wu, Yuming Du, Xiaosong Li, Yaru Tai, Huiling Su, Yuanjie. (2019). Optimization of temperature uniformity of a serpentine thin film heater by a two-dimensional approach. Microsystem Technologies. 25. 10.1007/s00542-018-3932-0.

[26] Gutruf, Philipp Walia, Sumeet Ali, Md Sriram, Sharath Bhaskaran, Madhu. (2014). Strain response of stretchable micro-electrodes: Controlling sensitivity with serpentine designs and encapsulation. Applied Physics Letters. 104. 10.1063/1.4862264.

[27] S. L. Firebaugh, K. F. Jensen, and M. A. Schmidt, “Investigation of high-temperature degradation of platinum thin films with an in situ resistance measurement apparatus,” J. Microelectromech. Syst., vol. 7, no. 1, pp. 128–135, Mar. 1998. [Online]. Available: http://ieeexplore.ieee.org/stamp/stamp.jsp?arnumber=661395

[28] S. Z. Ali, F. Udrea, W. I. Milne, and J. W. Gardner, “Tungsten-based SOI microhotplates for smart gas sensors,” J. Microelectromech. Syst., vol. 17, no. 6, pp. 1408–1417, Dec. 2009. [Online]. Available: https://www.researchgate.net/publication/224349026 TungstenBased SOI Microhotplates for Smart Gas Sensors

[29] Srinivasan R, Hsing I, Berger PE, Jensen KF, Firebaugh SL, Schmidt MA, Harold MP, Lerou JJ, Ryley JF (1997) Micromachined reactors for catalytic partial oxidation reactions. AIChE J 43:3059–3069

[30] Tiantian Zhang, Li Jia, Lixin Yang, Yogesh Jaluria, Effect of viscous heating on heat transfer performance in microchannel slip flow region, International Journal of Heat and Mass Transfer, Volume 53, Issues 21–22, 2010, Pages 4927-4934, ISSN 0017-9310, https://doi.org/10.1016/j.ijheatmasstransfer.2010.05.055.

[31] Ye, Jiamin Peng, Lihui Wang, Weirong Zhou, Wenxing. (2011). Optimization of Helical Capacitance Sensor for Void Fraction Measurement of Gas-Liquid Two-Phase Flow in a Small Diameter Tube. IEEE Sensors Journal - IEEE SENS J. 11. 2189-2196. 10.1109/JSEN.2011.2116115.

[32] Pieter Gijsenbergh, Maarten Driesen, Philippe Jourand, Robert Puers, Integrated Void Fraction Sensors for Two-phase, Microfluidic Systems, Procedia Engineering, Volume 47, 2012, Pages 643-646, ISSN 1877-7058, https://doi.org/10.1016/j.proeng.2012.09.229.

[33] M. bekker,Capacitive measurement technique for void fraction measurements in two phase pipe flow Bachelor project final report

[34] Basso, Daniele Castello, Daniele Baratieri, Marco Fiori, L.. (2013). Hydrothermal Carbonization of Waste Biomass: Progress Report and Prospect.

[35] A. V. Mamishev, K. Sundara-Rajan, Fumin Yang, Yanqing Du and M. Zahn, "Interdigital sensors and transducers," in Proceedings of the IEEE, vol. 92, no. 5, pp. 808-845, May 2004, doi: 10.1109/JPROC.2004.826603.

[36] Duan, Zhipeng Yovanovich, M.. (2009). Pressure Drop for Laminar Flow in Microchannels of Arbitrary Cross-Sections. Annual IEEE Semiconductor Thermal Measurement and Management Symposium. 111 - 120. 10.1109/STHERM.2009.4810751.

[37] Henning AK, Patel S, Selser M, Cozad BA (2004) Factors affecting silicon membrane burst strength. Proc SPIE 5343:145–153

[38] Henning AK, Patel S, Selser M, Cozad BA (2004) Factors affecting silicon membrane burst strength. Proc SPIE 5343:145–153

[39] Ngo HD, Tham AT, Simon A, Obermeier E (2008) Corner rounding to strengthen silicon pressure sensors using DRIE. In: Proceedings of the IEEE sensors conference, pp 1576–1579

[40] Tanaskovic´ D, Djuric´ Z, Lazic´ Z (1995) Influence of impurity distribution on thermal coefficients of resistivity and piezoresistivity of diffused layers of silicon. In: Proceedings of the 20th international conference on microelectronics (MIEL'95), vol 2, p 573

[41] Richter J (2008) Piezoresistance in microsystems. PhD thesis, DTU Nanotech

[42] Kuo Huan Peng, C. M. Uang, and Yih Min Chang "The temperature compensation of the silicon piezoresistive pressure sensor using the half-bridge technique", Proc. SPIE 5343, Reliability, Testing, and Characterization of MEMS/MOEMS III, (23 December 2003); https://doi.org/10.1117/12.527387

[43] Kumar, S. Pant, Bikram. (2014). Polysilicon thin film piezoresistive pressure microsensor: design, fabrication and characterization. Microsystem Technologies. 21. 10.1007/s00542-014-2318-1.

[44] Mallon Jr, J. R., F. Pourahmadi, K. Petersen, P. Barth, T. Vermeulen and J. Bryzek (1990). Low-pressure sensors employing bossed diaphragms and precision etch stopping. Sensors and ActuatorsA: Physical, 21(1-3), 89–95.

[45] M. Abassi P. Enoksson S. Rahiminejad, P. Cegielski. A four level silicon microstructure fabrication by drie. Journal of Micromechanics and Microengineering, 2016.

[46] N. K. Poon, B. M. H. Pong and C. K. Tse, "A constant-power battery charger with inherent soft switching and power factor correction," in IEEE Transactions on Power Electronics, vol. 18, no. 6, pp. 1262-1269, Nov. 2003, doi: 10.1109/TPEL.2003.818823.

[47] X. Wang Q. Li. A novel sandwich differential capacitive accelerometer with symmetrical double-sided serpentine beam-mass structure. Journal of Micromechanics and Microengineering, 2016.

A Appendix

FLOWCHART

Silicon Processing

Zero Layer
1. CLEANING: HNO3 99% and 69.5%
2. COAT 1.4 um EC3012 photoresist with EBR
3. ALIGNMENT AND EXPOSURE on the PAS5500/80 waferstepper
4. DEVELOP with Single Puddle process
5. INSPECTION: Pattern quality, linewidth and overlay
6. PLASMA ETCHING: Alignment markers (URK's) in Silicon
7. Photoresist removal in Oxygen plasma
8. INSPECTION: resist removal

Implantation
9. CLEANING: HNO3 99% and 69.5%
10. DRY OXIDATION: Channeling and Dirt barrier
11. MEASUREMENT: Oxide thickness
12. COAT 1.4 um EC3012 photoresist with EBR
13. ALIGNMENT AND EXPOSURE on the PAS5500/80 waferstepper
14. DEVELOP with Single Puddle process
15. INSPECTION: Pattern quality, linewidth and overlay
16. IMPLANTATION: Boron ions
17. LAYER STRIPPING: Photoresist
18. CLEANING:HNO399% and 69.5%
19. COAT 1.4 um EC3012 photoresist with EBR
20. ALIGNMENT AND EXPOSURE on the PAS5500/80 waferstepper
21. DEVELOP with Single Puddle process
22. INSPECTION: Linewidth and overlay
23. IMPLANTATION: Boron ions
24. Photoresist removal in Oxygen plasma
25. ANNEALING

Interconnect
26. CLEANING:HNO_3 99%
27. PECVD TEOS DEPOSITION
28. Measure oxide thickness
29. COAT 1.4 um EC3012 photoresist with EBR
30. ALIGNMENT AND EXPOSURE on the PAS5500/80 waferstepper
31. DEVELOP with Single Puddle process
32. WET ETCHING: Oxide etch
33. PHOTORESIST REMOVAL IN ACETONE
34. CLEANING:HNO399%
35. WET ETCHING: Oxide dip etch
36. AL SPUTTERING
37. CLEANING: HNO3 99%
38. COAT 1.4 um EC3012 photoresist with EBR
39. ALIGNMENT AND EXPOSURE on the PAS5500/80 waferstepper
40. DEVELOP with Single Puddle process
41. INSPECTION: Pattern quality, linewidth and overlay
42. WET ETCHING: Aluminium etch
43. PHOTORESIST REMOVAL IN ACETONE (PHOTRESIST STRIP)

BACK SIDE HARD MASK
44. CLEANING PROCEDURE: HNO3 100%

45. PECVD TEOS DEPOSITION (HARD MASK)
46. COAT 1.4 um EC3012 photoresist with EBR
47. ALIGNMENT AND EXPOSURE on the PAS5500/80 waferstepper
48. DEVELOP with Single Puddle process
49. INSPECTION: Linewidth and overlay
50. Dry Etching PECVD TEOS
51. MEASUREMENT: TEOS THICKNESS

FRONTSIDE RECESS

52. CLEANING PROCEDURE: HNO3 100%
53. COAT 10 um AZ12XT photoresist
54. ALIGNMENT AND EXPOSURE on the PAS5500/80 waferstepper
55. DEVELOP with Double Puddle process
56. INSPECTION: Pattern quality, linewidth and overlay
57. DRIE
58. INSPECTION: 3D microscope analyser
59. Photoresist removal in Oxygen plasma

On-silicon heater and contact openings

60. CLEANING PROCEDURE: HNO3 100%
61. PECVD TEOS DEPOSITION
62. Ti SPUTTERING
63. LAYER SHEET RESISTANCE MEASUREMENT
64. Al Sputtering
65. CLEANING PROCEDURE: HNO3 100%
66. SPRAY COATING
67. ALIGNMENT AND EXPOSURE on the PAS5500/80 waferstepper
68. DEVELOP with Double Puddle process
69. INSPECTION: Linewidth and overlay
70. WET ETCHING: Aluminium etch
71. WET ETCHING: Poly-Silicon dip etch
72. CLEANING PROCEDURE: HNO3 100%
73. SPRAY COATING
74. ALIGNMENT AND EXPOSURE on the PAS5500/80 waferstepper
75. DEVELOP with Double Puddle process
76. DRY ETCHING (Titanium)
77. Photoresist removal in Oxygen plasma
78. CLEANING PROCEDURE: HNO3 100%
79. SPRAY COATING
80. ALIGNMENT AND EXPOSURE on the PAS5500/80 waferstepper
81. DEVELOP with Double Puddle process
82. INSPECTION: Linewidth and overlay
83. Dry Etching PECVD TEOS
84. LAYER STRIPPING: Photoresist
85. CLEANING PROCEDURE: HNO3 100%
86. COAT 10 um AZ12XT photoresist

BACKSIDE softmask and two step etch

87. COAT 10 um AZ12XT photoresist
88. ALIGNMENT AND EXPOSURE on the PAS5500/80 waferstepper
89. DEVELOP with Double Puddle process
90. DRIE
91. INSPECTION: 3D microscope analyzer
92. Photoresist removal in Oxygen plasma
93. DRIE
94. BHF wet etching (Backside Hard Mask removal)

GLASS Processing

1.Ti sputtering

2.Al sputtering
3.COAT 1.4 um EC3012 photoresist with EBR
4.ALIGNMENT AND EXPOSURE on the PAS5500/80 waferstepper
5.DEVELOP with Single Puddle process
6.Wet etch aluminum
7.PHOTORESIST REMOVAL IN ACETONE
8.COAT 1.4 um EC3012 photoresist with EBR
9.ALIGNMENT AND EXPOSURE on the PAS5500/80 waferstepper
10.DEVELOP with Single Puddle process
11.Dry Etching Ti
12.Photoresist removal in Oxygen plasma
13. PECVD TEOS DEPOSITION
14.COAT 1.4 um EC3012 photoresist with EBR
15.ALIGNMENT AND EXPOSURE on the PAS5500/80 waferstepper
16.DEVELOP with Single Puddle process
17.Dry Etching PECVD TEOS
18. Photoresist removal in Oxygen plasma

B Appendix

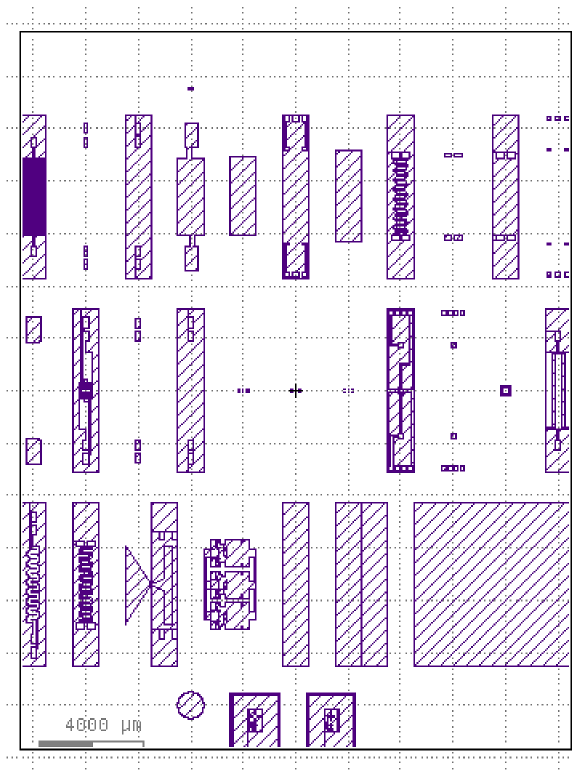

Figure 60: Mask layout